SNO+ and Geoneutrino Physics

by

Chunlin Lan

A thesis submitted to the Department of Physics, Engineering Physics and Astronomy
in conformity with the requirements
for the degree of Master of Science

Queen's University
Kingston, Ontario, Canada
February 2007

ABSTRACT

The SNO+ detector and physics goals are described. A reference model of the Earth was built for geoneutrino calculations. Based on this model, the geoneutrino flux and spectrum at SNOLAB were calculated after a study of the antineutrino spectra of ^{238}U chains and ^{232}Th chains and the propagation of antineutrinos in the Earth affected by matter oscillations. The estimated geoneutrino event rate in SNO+ is 49 events per 10^{32} proton-years. As one of the backgrounds, the flux and spectrum of $\bar{\nu}_e$ from nuclear power plants were also studied and the event rate within the range from 1.8 to 3.3 MeV is 44 events/10^{32} proton-years.

Internal backgrounds in the detector for geoneutrino detection were estimated. In case that the SNO+ scintillator were contaminated with ^{210}Pb at the level of KamLAND scintillator, the (α, n) $\bar{\nu}_e$ fake event rate in SNO+ would be about 106 events/10^{32} proton-years. To eliminate this background, a method of liquid scintillator purification by vacuum distillation was examined. The efficiency for removing ^{212}Pb is above 99.85%. Vacuum distillation of SNO+ scintillator would effectively eliminate internal background from (α, n). The optical transparency of liquid scintillator is also improved by vacuum distillation.

The geoneutrino signal to reactor background ratio in SNO+ was found to be about 4 times better than in KamLAND.

ACKNOWLEDGEMENTS

First of all, I would like to thank my supervisor, Dr. Mark Chen for all his help, guidance, and financial support in the past two years. I appreciate his encouragement when I made even small advancements and his patience when my research did not go as expected. Many thanks to Dr. Aksel Hallin for numerous help and his guidance, especially in my first year. Thanks to Dr. Ian Towner for his patient help for both my thesis and courses.

Thanks to Xin Dai and Eugene Guillian, whose discussion and information were always very helpful. Many thanks to: Alex Wright, Chris Howard, Mark Kos, Ryan Martin, Ryan Maclellan, Carsten and Christine for answering my numerous questions in all areas, physics or not. They make the offices in the basement full of fun as well as science. Thanks to Peter Skensved and Steve Gillen for their assistance when I encountered computer problems and their other help. Thanks to Dr. Barry Robertson, Dr. Hugh C. Evans and Dr. Hamish Leslie for lending me their books, instruments and giving me useful references.

CONTENTS

LIST OF FIGURES

LIST OF TABLES

Chapter 1. INTRODUCTION

1.1 A Brief Description of SNO

The famous Sudbury Neutrino Observatory (SNO) is located near Sudbury, Ontario, Canada 6800 feet underground in INCO's Creighton mine. This location is great for experiments which require very low cosmic ray backgrounds because the 6800 feet of rock overburden is ideal shielding for cosmic rays. This depth is much greater than most of the other underground labs in the world therefore it provides much better shielding. The SNO experiment continued taking data until December 2006. It is a huge water Cherenkov neutrino detector with 1000 tons of heavy water as the sensitive target material. The main physics goal of SNO is to judge if the electron neutrinos originating from the Sun oscillate into other flavours when they fly to the Earth. Because the solar neutrinos are originally electron flavour, if the electron neutrino flux at the Earth is less than the total neutrino flux at the same location of the Earth, we can say that some of the electron neutrinos changed their flavour or the neutrinos undergo flavour oscillations. Other solar neutrino experiments were not able to make this judgment because they could only detect electron neutrinos but not the other flavours.

SNO has the ability to detect all three flavours of the neutrinos through the following reactions:

Charged Current, or CC

$$\nu_e + d \longrightarrow p + p + e^- \tag{1.1}$$

Neutral Current, or NC

$$\nu_x + d \longrightarrow p + n + \nu_x \tag{1.2}$$

Elastic Scattering, or ES

$$\nu_x + e^- \longrightarrow \nu_x + e^- \tag{1.3}$$

where ν_x refers to any flavour of neutrino. The CC reaction is sensitive only to electron neutrinos, while the neutral current reaction is equally sensitive to all active neutrino flavours. Thus the CC reaction is good for an electron neutrino flux measurement and the NC reaction is good for the total neutrino flux measurement. The elastic scattering reaction is sensitive to all flavours, but with relatively lower sensitivity to ν_μ and ν_τ than to ν_e. The CC reactions produce electrons (ES reactions scatter electrons), and then the electrons produce Cherenkov light, which can be collected by the photomultiplier (or PMT) array on the inner side of the detector sphere. The NC reaction produces neutrons. The neutrons can be captured by nuclei and release one or more γ photons, and then the γ photons interact with electrons via Compton scattering. Cherenkov light is produced by these scattered electrons. This was the mechanism for detecting the NC reaction in the first and second phases of SNO.

The structure of the SNO detector is shown in Figure 1.1 and Figure 1.2. As indicated in Figure 1.1, the 12 meter diameter spherical acrylic vessel contains 1000 ton of ultra-pure heavy water and it is contained within a Photomultiplier SUPport structure (PSUP). Ultra-pure light water was put between the acrylic vessel and the PSUP to shield the acrylic vessel from surrounding radiations. There are about 9,500 photomultipliers attached on the inner side of the PSUP. Ultra-pure light water fills the cavity outside the PSUP. Because heavy water is denser than normal light water,

the acrylic vessel must be hung by suspension ropes.

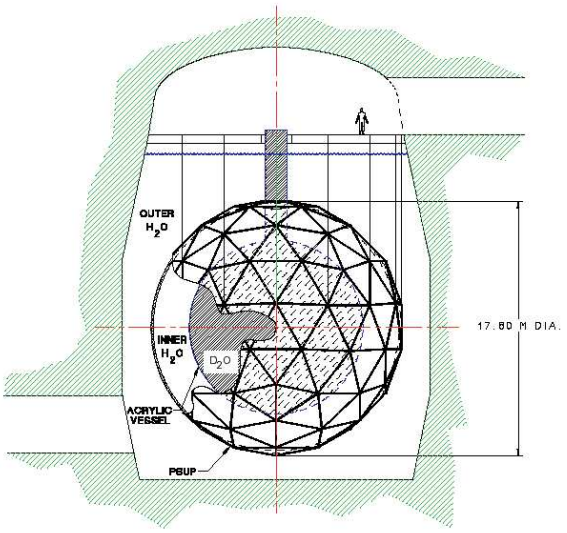

Figure 1.1: The PMT support structure (PSUP) shown inside the cavity, surrounding the acrylic vessel, with light water outside the vessel and heavy water inside the vessel.

The SNO detector structure in Phase III is shown in Figure 1.2. In addition to the structures described above, ^{3}He proportional counters were placed in the acrylic vessel. These counters count the neutrons produced by the Neutral Current reactions, so they are also called "Neutral Current Detectors" or NCDs.

SNO has precisely measured the ν_e flux and the non-ν_e flux, and finally confirmed solar neutrino oscillations[1]. Including the measurements of other experiments, the best-fit values for the two-neutrino mixing parameters are $\Delta m^2 = 8.0^{+0.6}_{-0.4} \times 10^{-5} eV^2$ and $\theta = 33.9^{+2.4}_{-2.2}$ degrees[2].

1.2 The Detector of SNO+

After the SNO experiment, a new experiment, SNO+ will be started. The infrastructure of the SNO+ detector will be built using the previous SNO hardware including the cavity, the PSUP, the photomultiplier tube array, the acrylic vessel and so on.

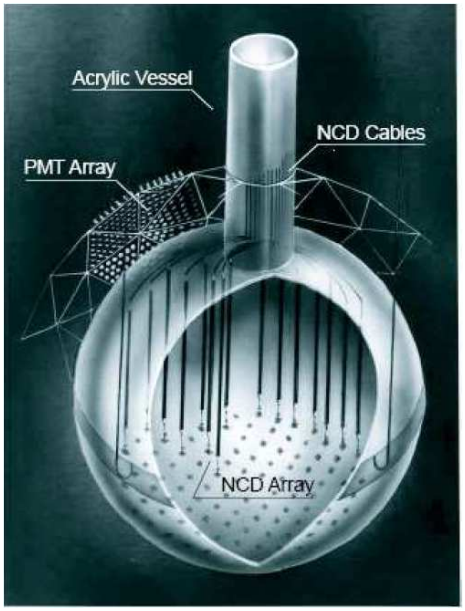

Figure 1.2: An artist's image of SNO with the NCD array

The main modification of the detector from the original SNO detector is the replacement of the heavy water by liquid scintillator. Some other modifications are also needed, for example, the acrylic vessel must be attached to the bottom of the cavity and not hung from the top of the cavity because the liquid scintillator is lighter than water.

The SNO+ detector detects $\bar{\nu}_e$'s via inverse β-decay. The threshold of this reaction is 1.804 MeV.

$$\bar{\nu}_e + p \longrightarrow e^+ + n \tag{1.4}$$

This reaction has a well-established cross-section as a function of E_ν, the energy of the $\bar{\nu}_e$. The kinetic energy of the positron is $E_\nu - 1.804$ MeV. The positron annihilates an electron immediately and produces 2 γ photons and then deposits $E_\nu -$ 0.8 MeV energy in the detector. One can consider this event as the prompt event. After a mean time of $\sim$ 200 μs, the neutron is captured by a proton, and then produces a deuteron and a 2.2 MeV γ photon. The detection of the scintillation

light from the scattered electrons by this 2.2 MeV γ photon is a delayed event. The spatial and temporal coincidence between the prompt event and the delayed event provide a distinctive signal that helps limit backgrounds.

SNO+ detects neutrinos through the following Elastic Scattering interaction,

$$\nu_x + e^- \longrightarrow \nu_x + e^- \tag{1.5}$$

This interaction is more sensitive to electron neutrinos than other flavours, although it can detect all flavours. The kinetic energy of the scattered electron may be any value between 0 and the kinematic upper limit which is slightly less than the energy of the neutrino. Knowledge of the differential scattering cross section of this interaction allows extraction of the neutrino spectrum from the scattered electron spectrum.

1.3 The Physics Purpose of SNO+

SNO+ will have a lower energy threshold than that of SNO because of the higher light output of liquid scintillator compared with Cherenkov light in water. SNO+ will be able to access low energy solar neutrino physics because of this lower energy threshold including sensitivity to pep neutrinos ($p + e^- + p \rightarrow {}^2\mathrm{H} + \nu_e$), ^{7}Be and CNO solar neutrinos [3]. Physics with antineutrinos, such as geoneutrino physics and reactor antineutrino measurements are also goals of SNO+.

1.3.1 Geoneutrino Physics

β^- decays are the source of $\bar{\nu}_e$. In the Earth, there are two plentiful natural decay chains, the ^{238}U chain and the ^{232}Th chain, that produce $\bar{\nu}_e$s above the energy threshold 1.804 MeV. ^{40}K is also a plentiful natural $\bar{\nu}_e$ source, but the maximum energy of the $\bar{\nu}_e$ is less than 1.804 MeV and cannot be detected by SNO+. There is also ^{235}U

in the Earth. Though the natural abundance of ^{235}U is 0.72%, the neutrino flux it produces is about 3% of the neutrino flux from ^{238}U [4]. While this is non-negligible, it will also be ignored in this thesis as the antineutrinos from ^{235}U have less than 1.8 MeV maximum energy. In the rest of this thesis, uranium will be taken as ^{238}U. The $\bar{\nu}_e$s produced in natural decays within the Earth are called geoneutrinos.

Geoneutrinos are probes of the deep Earth because they are rarely absorbed on their way from their place of origin to detectors near the surface. The flux and the spectrum of geoneutrinos reflect the amount and the distribution of the relative isotopes in the Earth. Geoneutrino detection also offers a possible way to estimate the radiogenic power contributing to the Earth's heat.

1.3.2 Reactor Antineutrino Physics

In nuclear power plants, the fission products undergo β^- decay and produce lots of $\bar{\nu}_e$s. The flux of $\bar{\nu}_e$ depends on the thermal power of the reactors and the composition of the fuel [5] [6]. The $\bar{\nu}_e$ spectrum depends on the fuel composition. Both the flux and the spectrum are well studied[5][6], so reactors are good sources for neutrino oscillation parameter measurements. There is a reactor neutrino experiment in Japan called KamLAND that measured the oscillation parameters [7] [8] using this method. KamLAND is a 1000 tonne liquid scintillator detector located in Kamioka, Japan. It is very similar to what SNO+ would be. As such, KamLAND's signals and backgrounds will be referred to often in this thesis, for comparison with SNO+. All over Japan, nuclear power reactors produce $\bar{\nu}_e$ that were detected at an effective baseline of 180 km by the KamLAND detector. The Bruce nuclear generating station is 240 kilometers away from SNO+ while Pickering and Darlington nuclear power plants are about 340 kilometers away. The oscillation wavelength of several MeV $\bar{\nu}_e$s is about 100 kilometers. SNO+ can measure the neutrino oscillation parameters and confirm the results of KamLAND.

1.3.3 Solar Neutrino Physics

Because SNO+ is sensitive to low energy solar neutrinos and can measure the low energy neutrino spectrum, solar physics and neutrino physics can be studied. It is possible that SNO+ would detect pep neutrinos, ^{7}Be neutrinos and CNO neutrinos for the first time. Besides these possible firsts, SNO+ can also provide qualitative and quantitative evidence of the MSW (Mikheyev, Smirnov, Wolfenstein) [9] effect, resulting from neutrino oscillations in matter. Figure 1.3 shows the calculated survival probability of solar neutrinos as a function of energy. In the low energy range, there is an upturn. The low energy threshold of SNO+ makes it possible to check this prediction of the "LMA MSW" model of neutrino oscillations.

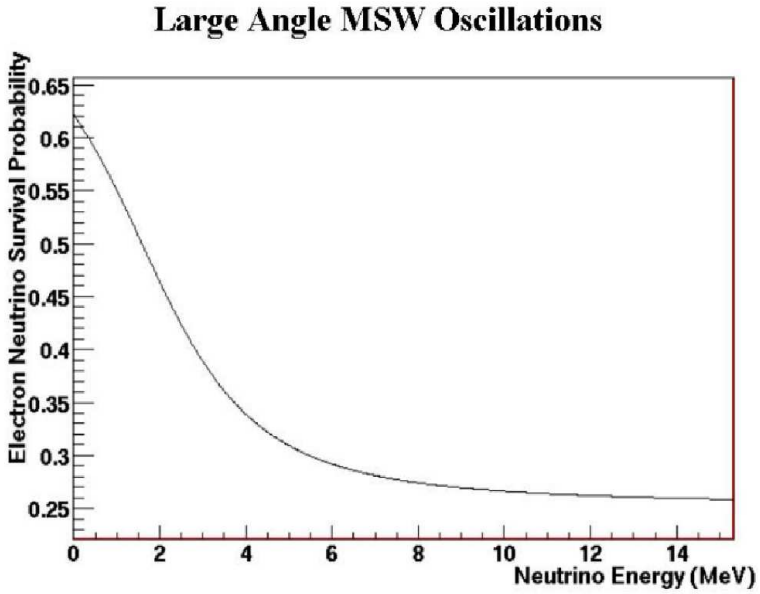

Figure 1.3: The survival probability of solar neutrinos due to large angle MSW oscillations

SNO+ has the unique ability to measure the precisely predicted pep neutrino flux. Because the pep neutrino flux is large enough to produce a high event rate, a statistically precise measurement is possible. This would not only provide an improved measurement of neutrino oscillation parameters, but would also provide information about new physics including sterile neutrinos, non-standard neutrino-

matter interactions and CPT symmetry [10].

1.3.4 Supernova Neutrinos

The connection between supernova explosions and neutrino bursts was confirmed by Kamiokande II and the Irvine-Michigan-Brookhaven (IMB) Collaborations in 1987 [11] [12], with SN 1987A, a type II supernova that occurred about 50kpc away from the Earth in the Large Magellanic Cloud. The detected gross energetics, the characteristic duration and the significant electron antineutrino content of SN 1987A were consistent with the supernova explosion models developed in the 1980s [13]. Because there were only 19 events collected by the IMB and Kamiokande II detectors, the important details of those models could not be confirmed. The data have also been used for testing neutrino oscillation models[14], setting limits on neutrino mass [15] and constraining the size of compact dimensions [16].

SNO+ is a good supernova neutrino detector. It is calculated that SNO+ would detect about 645 neutrino events if a 3×10^{53} erg supernova exploded 10kpc away from the Earth[17]. SNO+ will have the ability to differentiate the flavours of the detected neutrinos because it detects the neutrinos through several different interactions which are more sensitive to some flavours than to others[17], therefore the data can offer more detailed information about both the supernova explosion mechanism and neutrino physics than previous experiments.

1.3.5 Neutrinoless Double β Decay

Whether neutrinos are Majorana or Dirac particles is one of the most important open questions in neutrino physics. A Dirac particle is distinct from its anti-particle while a Majorana particle is identical to its anti-particle except for their helicities. A Majorana particle can act as its own anti-particle experimentally. Considering a double β decay process,

$$(A, Z) \longrightarrow (A, Z+2) + 2e^- + 2\bar{\nu} \tag{1.6}$$

if neutrinos are Majorana particles, one of the two antineutrinos could be absorbed by the other one as a neutrino, and the reaction becomes

$$(A, Z) \longrightarrow (A, Z+2) + 2e^- \tag{1.7}$$

This reaction is a neutrinoless double β decay. If this reaction is observed, then it's confirmed that neutrinos are Majorana particles. Since the rate of neutrinoless double decay is related to neutrino mass [18], the observation also provides a measurement of the neutrino mass.

Double beta decay isotopes might be loaded in the SNO+ liquid scintillator. One advantage of SNO+ to search for neutrinoless double β decay is that the total mass of liquid scintillator in the detector will be at the kiloton level, allowing the total mass of the isotope used to be very large compared to existing double β decay experiments. Although the energy resolution of the SNO+ detector might not be as good as other experiments, the large statistics due to the large amount of isotope used would allow some ability to separate the 2 $\bar{\nu}$ events from the neutrinoless events.

1.4 Outline of this Thesis

This chapter has introduced the physics goals of SNO+ and described the existing SNO detector. In this thesis, the focus will be on geoneutrino physics in SNO+. An Earth model will be built for geoneutrino flux and spectrum calculations. The distribution of $\bar{\nu}$ sources, uranium and thorium, and the $\bar{\nu}$ spectra of uranium decay chain and thorium decay chain will be discussed. Propagation of $\bar{\nu}$ in the Earth was an important aspect to study. The geoneutrino flux and spectrum were calculated based on these studies. As the most significant background, the $\bar{\nu}$ flux and spectrum

from nuclear plants were also calculated and are discussed in this chapter.

The internal background of SNO+ will be studied in Chapter 3. For geoneutrino detection, the most important internal background is fake $\bar{\nu}$ events caused by (α, n) neutrons. This background will be estimated. In order to reduce internal backgrounds, purification of liquid scintillator was examined, and in particular a method to remove backgrounds from ^{210}Pb which is the most problematic source of fake $\bar{\nu}$ events, was developed.

Conclusions are presented in the last chapter of this thesis.

Chapter 2. GEONEUTRINO PHYSICS IN SNO+

Eder[19] and Marx[20] first suggested to study the inner Earth using $\bar{\nu}_e$s originating from the Earth's natural radioactivity. This idea has been reviewed many times later[21] [22] [23] [24] [25] [26]. In 2005, the KamLAND Collaboration announced that they detected geoneutrinos for the first time. The 90% confidence interval of their detection was from 4.5 to 54.2 geoneutrino events (this assumed a Th/U mass concentration ratio of 3.9). Using these data, they provided an upper limit of 60 TW for the radiogenic power of U and Th in the Earth [27], though arguments made in [28] suggest the limit is more like 160 TW.

We expect to do a statistically better measurement of geoneutrinos in SNO+. SNOLAB is a good location for geoneutrino detection. The first advantage is that the geoneutrino flux at SNOLAB is higher than at KamLAND. This is because thick continental crust surrounds SNOLAB. Near KamLAND, there is oceanic crust which has much lower concentrations of U and Th compared to continental crust. The second advantage is that the $\bar{\nu}_e$ background at SNOLAB from nuclear power plants is about 4 times lower than at KamLAND. Nuclear power is extensively used in Japan and plants are near the KamLAND site - KamLAND is foremost a reactor neutrino experiment. We also expect to reduce the $^{13}\mathrm{C}(\alpha, n)^{16}\mathrm{O}$ background, which is the main internal background for $\bar{\nu}_e$ detection. The SNO+ Collaboration is developing effective methods to purify the liquid scintillator and aims to make this background at SNO+ lower than that of KamLAND. A better measurement is possible enabling

extraction of new information about the deep Earth.

2.1 Overview of the Geoneutrino Flux and Spectrum Calculation

The geoneutrino spectrum and flux at SNOLAB depend on three factors: the spatial distribution of sources, the spectrum of $\bar{\nu}_e$ of the sources and the survival probability of the $\bar{\nu}_e$ traveling from the source to the lab. The following discussions about the three factors are in a spherical coordinate system.

To describe the distribution of geoneutrino sources, we can define the $\bar{\nu}_e$ yield per unit volume at a position (θ, ϕ, r) as $S(\theta, \phi, r)$, where θ is the latitude, ϕ is the longitude and r is the distance from the center of the Earth.

The $\bar{\nu}_e$ spectrum of the sources will depend upon the radioactive isotope content at each location and we describe the spectrum as a function of energy $\Phi(E)$.

The survival probability of an electron $\bar{\nu}_e$ depends on its energy, the distance it must travel and the electron density along the travel path. For a given source position within the Earth, the distance and the path to the lab are known. In other words, the distance and the path are functions of the source location. Therefore, the survival probability of the $\bar{\nu}_e$ propagating from the source (θ, ϕ, r) to the site can be described as a function of the source location and the energy of the $\bar{\nu}_e$, $P_{ee}(\theta, \phi, r, E)$. The flux of geoneutrinos within an energy range from E to $E + dE$ originating from a differential volume element dv at the position (θ, ϕ, r) is:

$$df = \frac{1}{4\pi \left|\vec{r_o} - \vec{r}\right|^2} S(\theta, \phi, r)\Phi(E)P_{ee}(\theta, \phi, r, E)dvdE \tag{2.1}$$

where $dv = dr(rd\theta)(r\cos\theta d\phi)$ and $|\vec{r_o} - \vec{r}|$ is the distance from the source to the observatory lab, so that

$$df = \frac{1}{4\pi \left|\vec{r_o} - \vec{r}\right|^2} S(\theta, \phi, r)\Phi(E)P_{ee}(\theta, \phi, r, E)r^2 \cos\theta dr d\theta d\phi dE \quad (2.2)$$

The spectrum of geoneutrinos at the site is:

$$\begin{aligned} f(E) &= \int_0^{R_{earth}} \int_{-\pi/2}^{\pi/2} \int_{-\pi}^{\pi} \frac{1}{4\pi \left|\vec{r_o} - \vec{r}\right|^2} S(\theta, \phi, r)\Phi(E)P_{ee}(\theta, \phi, r, E)r^2 \cos\theta dr d\theta d\phi \\ &= \Phi(E) \int_0^{R_{earth}} \frac{r^2}{4\pi \left|\vec{r_o} - \vec{r}\right|^2} \int_{-\pi/2}^{\pi/2} \cos\theta \int_{-\pi}^{\pi} S(\theta, \phi, r)P_{ee}(\theta, \phi, r, E) dr d\theta d\phi \end{aligned} \quad (2.3)$$

and the geoneutrino flux at the site is:

$$\begin{aligned} f &= \int_0^{E_{max}} f(E) dE \\ &= \int_0^{E_{max}} \Phi(E) \int_0^{R_{earth}} \frac{r^2}{4\pi \left|\vec{r_o} - \vec{r}\right|^2} \int_{-\pi/2}^{\pi/2} \cos\theta \int_{-\pi}^{\pi} S(\theta, \phi, r)P_{ee}(\theta, \phi, r, E) dE dr d\theta d\phi \end{aligned} \quad (2.4)$$

The following sections will discuss the three factors, the source distribution $S(\theta, \phi, r)$, the energy spectrum $\Phi(E)$ and the survival probability of geoneutrinos $P_{ee}(\theta, \phi, r, E)$ in detail.

2.2 A Model of the Earth

To estimate the geoneutrino flux and spectrum at SNOLAB, we have to study the geoneutrino source distribution and neutrino propagation in the Earth. Because the geoneutrinos originate from β^- decays, we are concerned with the distribution of β^- decay isotopes. The matter distribution also affects the flux and spectrum by affect-

ing the propagation of neutrinos, known as the Mikheyev-Smirnov-Wolfenstein effect [9]. This section shows a reference of the Earth, including the matter distribution and the distribution of ^{232}Th and ^{238}U, two decay chains which emit $\bar{\nu}_e$s above the reaction energy threshold of SNO+.

2.2.1 The Structure and Matter Distribution of the Earth

The Preliminary Reference Earth Model (PREM), built by Dziewonski and Anderson in 1981[29], is the most widely used Earth model today. It is an averaged Earth model based on seismological analysis. The model describes the parameters, such as the matter density, as a function of the radius and it is spherically symmetric. From the surface to the center of Earth, according to PREM, the Earth consists of the following principal regions:

(1) ocean layer;

(2) crust;

(3) the mantle, including the region above the low velocity zone(LID), low velocity zone, region between the low velocity zone and the 400 kilometer discontinuity, transition zone between the 400 and 670 kilometer discontinuities and the lower mantle;

(4) the core, including the outer core and the inner core.

Table 2.1 shows the mass density of the Earth at different radii from the center of the Earth. Figure 2.1 is a plot corresponding to Table 2.1.

The anisotropy of the first few tens of kilometers near the Earth's surface, including the ocean layer and the crust, is so great that the model doesn't reflect the real structure at any point of the Earth in this range. Because of the significance of the crust in a calculation of the geoneutrino flux, a much more detailed model of this part of the Earth, Crust 2.0 built by Gabi Laske et al. [30] will be adapted in the estimation and will be discussed in the following section.

Table 2.1: The structure and the mass density of the Earth[29]

Region	Radius (km)	ρ (kg/m^3)
Inner Core	0.0	13088.48
	200.0	13079.77
	400.0	13053.64
	600.0	13010.09
	800.0	12949.12
	1000.0	12870.73
	1200.0	12774.93
	1221.5	12763.60
Outer Core	1221.5	12166.34
	1400.0	12069.24
	1600.0	11946.82
	1800.0	11809.00
	2000.0	11654.78
	2200.0	11483.11
	2400.0	11292.98
	2600.0	11083.35
	2800.0	10853.21
	3000.0	10601.52
	3200.0	10327.26
	3400.0	10029.40
	3480.0	9903.49
Lower Mantle	3480.0	5566.45
	3600.0	5506.42
	3630.0	5491.45
	3800.0	5406.81
	4000.0	5307.24
	4200.0	5207.13
	4400.0	5105.90
	4600.0	5002.99
	4800.0	4897.83
	5000.0	4789.83
	5200.0	4678.44
	5400.0	4563.07
	5600.0	4443.17
	5600.0	4443.17
	5701.0	4380.71
Transition Zone	5701.0	3992.14
	5771.0	3975.84
	5871.0	3849.80
	5971.0	3723.78
	5971.0	3543.25
	6061.0	3489.51
	6151.0	3435.78
Low Velocity Zone	6151.0	3359.50
	6221.0	3367.10
	6291.0	3374.71
LID	6291.0	3374.71
	6346.6	3380.76
Crust	6346.6	2900.00
	6356.0	2900.00
	6356.0	2600.00
	6368.0	2600.00
Ocean	6368.0	1020.00
	6371.0	1020.00

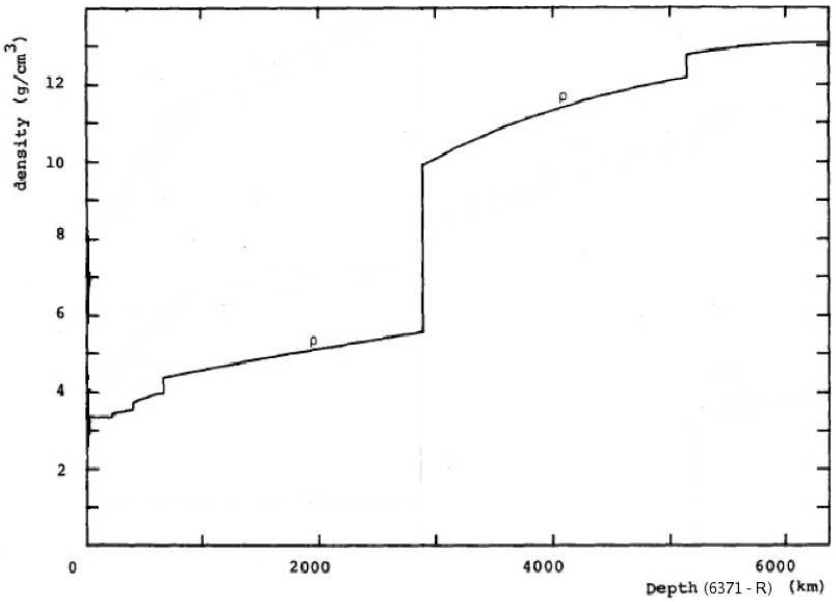

Figure 2.1: The mass density of the Earth[29]

2.2.2 Crust

The crust is the most significant geoneutrino source because the concentration of ^{238}U and ^{232}Th is much higher here than other parts of the Earth. To estimate the geoneutrino flux accurately, we need more detailed descriptions of the crust than that of the PREM.

The model CRUST 2.0 [30] describes the crust as a map with a resolution of 2 by 2 degrees. It is a part of the Reference Earth Model (REM), an upgrade of PREM being built by a community of geophysicists and geochemists. Crust 2.0 consists of 7 layers from the Earth surface to the bottom of the crust:

1. ice;
2. water;
3. soft sediment;
4. hard sediments;
5. upper crust;
6. middle crust and

7. lower crust.

The parameters of the 7 layers for every one of the 2 by 2 degree elements are given, including the velocity of an elastic P-wave, the velocity of an elastic S-wave, the thickness and the mass density. Figure 2.2 shows the thickness of the crust.

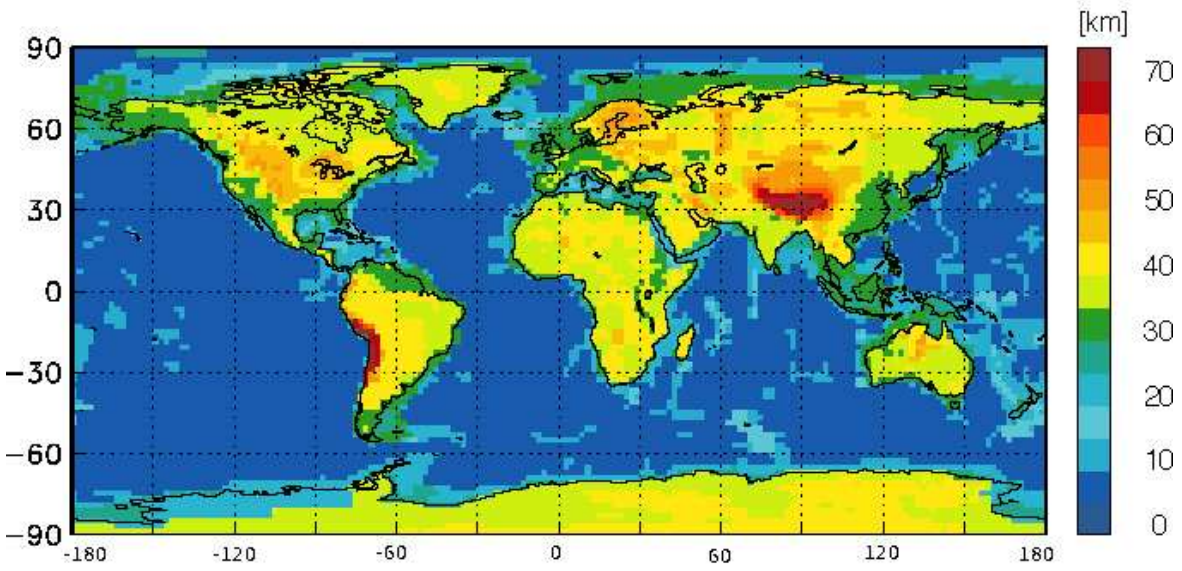

Figure 2.2: The thickness of the crust[30]

2.2.3 The Distribution of ^{238}U and ^{232}Th

The reaction energy threshold of SNO+ for $\bar{\nu}_e$ detection is 1.8 MeV. In the ^{238}U decay chain, ^{214}Bi has an 18% branch with a β^- endpoint of 3.27 MeV and ^{234}Pa has a β^- decay with an endpoint energy of 2.19 MeV. In the ^{232}Th decay chain, ^{228}Ac and ^{212}Bi have β^- decays with endpoint energies of 2.08 MeV and 2.25 MeV respectively. ^{235}U chain and ^{40}K also produce geoneutrinos but those are below the energy threshold for this reaction. The distribution of ^{238}U and ^{232}Th is one of the main factors affecting the geoneutrino flux.

In the earliest stages of the Earth, melting would have caused denser substances to sink toward the center while light materials migrate to the upper parts of the

Earth. This process is called planetary differentiation. As a result, the core is largely composed of iron, along with nickel and some light elements. Other dense elements, such as lead, thorium and uranium, either are too rare to be significant or tend to bind to lighter elements and thus flow up. It is believed that the core of Earth contains very little thorium and uranium compared to other parts of the Earth. The mantle is composed of silicate rocks. Although solid, the silicate material is ductile enough to flow on very long timescales because of the high temperatures within the mantle [31]. This property of the mantle makes it possible that uranium and thorium were carried to the crust by light elements they were attached to.

The distribution of U and Th in the Earth is summarized in [25] [27] [26] [32]. In our calculation, I adopt the latest compilation by Enomoto in [32]. The data and the references are tabulated in Table 2.2. The U and Th concentrations in the mantle are not known directly since sampling of true mantle rock cannot be done. Earth models start with the Bulk Silicate Earth model [25] which estimates the chemical composition of the whole Earth (based upon chondritic meteorites). Once the crust U and Th are distributed and determined from other sources, as given in Table 2.2, the mantle content is taken as the whole Earth content minus what's in the crust.

Table 2.2: The distribution of U and Th in the Earth

		U (PPM)	Th (PPM)	References
Sediment	Continental	2.8	10.7	Plank et al. (1998)[33]
	Oceanic	1.68	6.91	
Continental Crust	Upper	2.8	10.7	Rudnick et al.(1995)[34]
	Middle	1.6	6.1	
	Lower	0.2	1.2	
Oceanic Crust		0.10	0.22	Taylor et al.(1985)[35]
Mantle		0.012	0.048	
Core		0	0	McDonough(1999)[36]

The antineutrino flux from these two chains depends on the amount of the two isotopes and the distribution of them. In the case that the distribution is given,

the flux is proportional to the amounts. For given amounts of the two isotopes, the antineutrino flux depends on the distribution. For example, if large amounts of U and Th were partitioned in the core, it would result in a much smaller flux. If U and Th were not uniformly distributed in the mantle, but had a higher concentration in the upper mantle, this would result in a larger flux. There is the potential from a good geoneutrino measurement to be consistent with some models and inconsistent with others, helping to give some information on the U and Th distribution in the deep Earth.

2.3 $\bar{\nu}_e$ Spectrum of U and Th

A β^- decay emits an electron and an $\bar{\nu}_e$. The decay reaction can be expressed by the following equation

$$ {}^{A}_{Z-1}X \longrightarrow {}^{A}_{Z}Y + e^- + \bar{\nu}_e \tag{2.5} $$

Usually the daughter nucleus, ${}^{A}_{Z}Y$, has many excited states accessible in the β^- decay, so for each parent nucleus ${}^{A}_{Z-1}X$ there are several branches with different endpoint energies and branching ratios. The $\bar{\nu}_e$ spectrum of a given branch is

$$ \Phi(E_\nu) = \frac{30}{\Delta^5}[(\Delta - E_\nu)^2 - m_e^2]^{1/2}(\Delta - E_\nu)E_\nu^2 F(Z,(\Delta - E_\nu)) \tag{2.6} $$

where $F(Z,(\Delta - E_\nu))$ stands for the Fermi function, $\Delta = E_{endpoint} + m_e$, Z is the atomic number of the daughter isotope, m_e is the rest energy of an electron and E_ν is the $\bar{\nu}_e$ energy. Here $E_{endpoint}$ is the maximum kinetic energy for the electron, which in the case of the decay to the ground state is equal to the atomic mass difference of the parent and daughter nucleus. Given the branching ratios and endpoint energies we can calculate the $\bar{\nu}_e$ spectrum of a β^- decay by summing over the branches.

The ^{238}U decay chain is shown in Figure 2.3. There are six β^- decays in this

chain. The whole chain can be expressed by the following equation

$$^{238}U \longrightarrow^{206} Pb + 8^{4}He + 6e^{-} + 6\bar{\nu} + 51.7MeV \tag{2.7}$$

Figure 2.4 shows the ^{232}Th decay chain. The chain emits 4 $\bar{\nu}_e$s and can be expressed by the following equation.

$$^{232}Th \longrightarrow^{208} Pb + 6^{4}He + 4e^{-} + 4\bar{\nu} + 42.7MeV \tag{2.8}$$

The details of all decays in the two chains are given in [37] including the endpoints and branching ratios. On calculating the spectrum of each branch of the β^- decays with Equation 2.6 and summing over all branches we get the neutrino spectrum for the two chains as shown in Figure 2.5 and Figure 2.6.

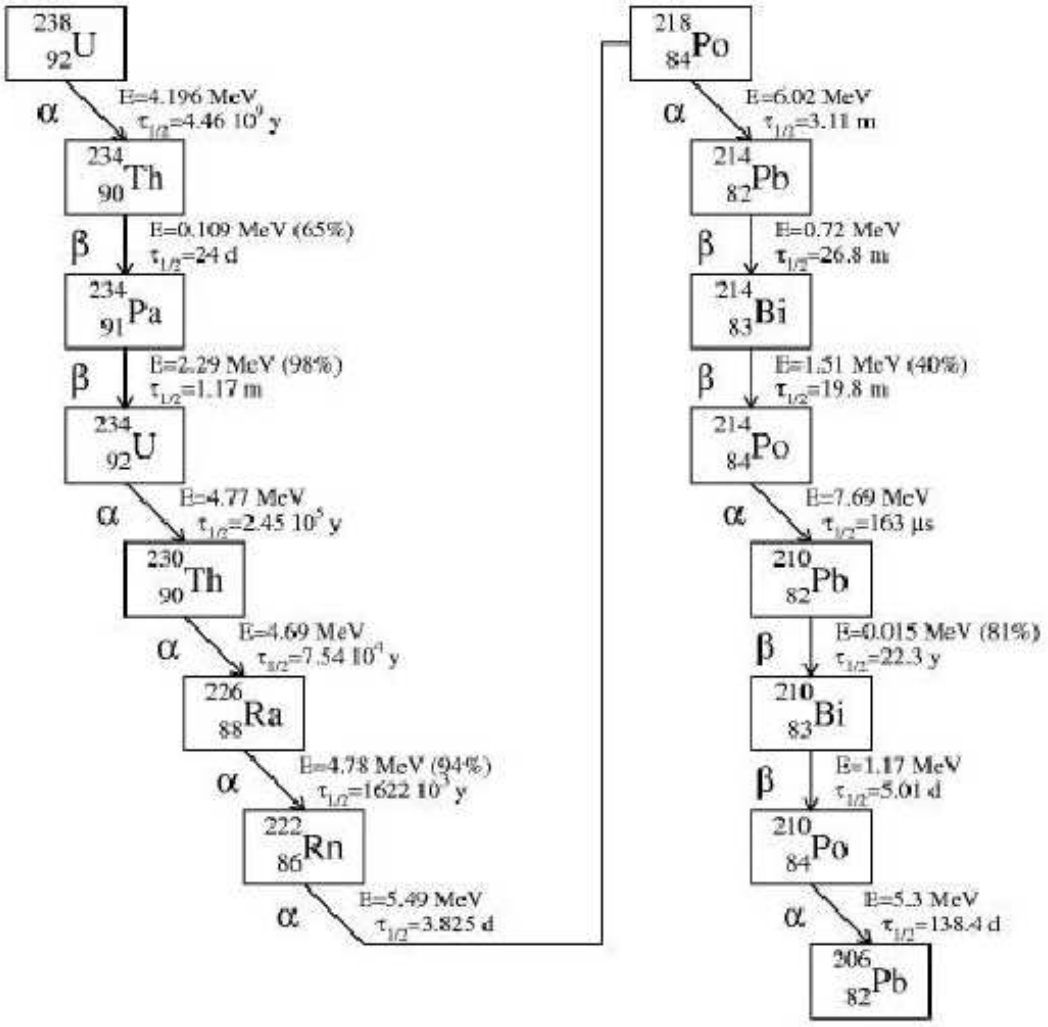

Figure 2.3: The decay chain of U

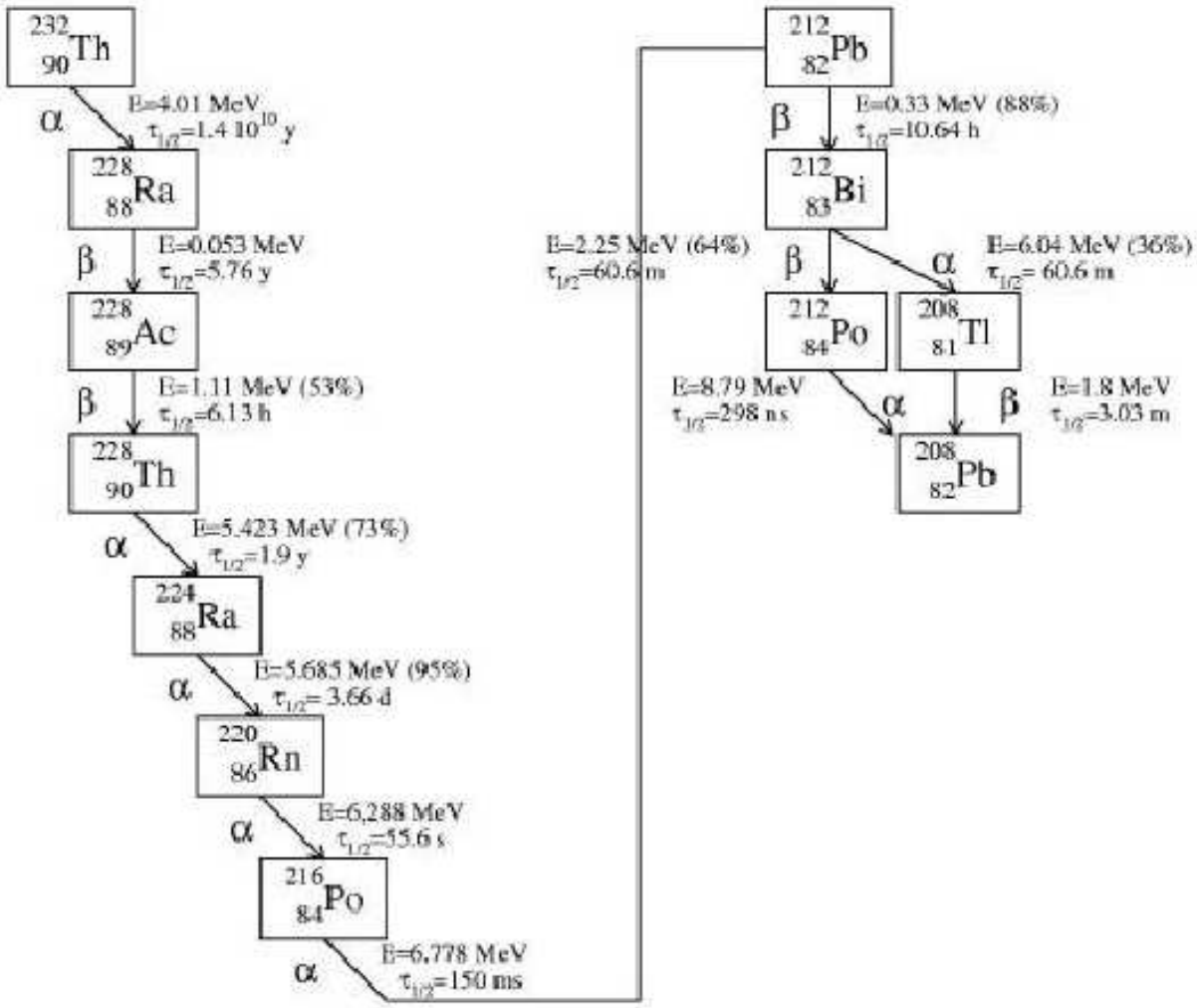

Figure 2.4: The decay chain of Th chain

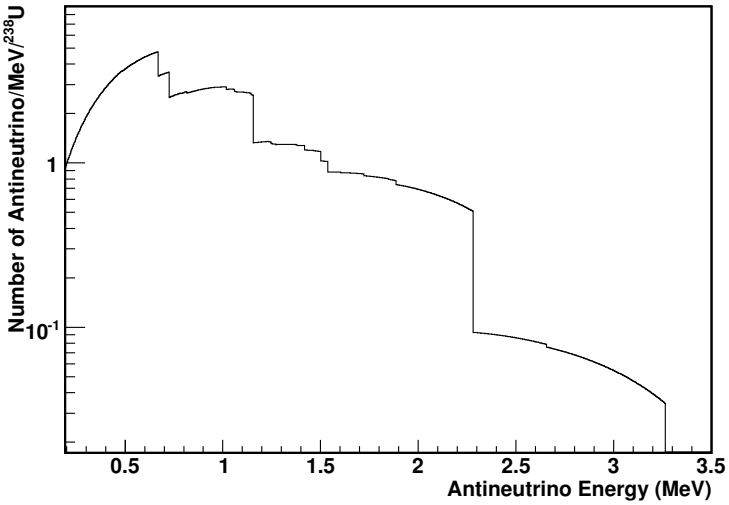

Figure 2.5: The $\bar{\nu}_e$ spectrum of U chain

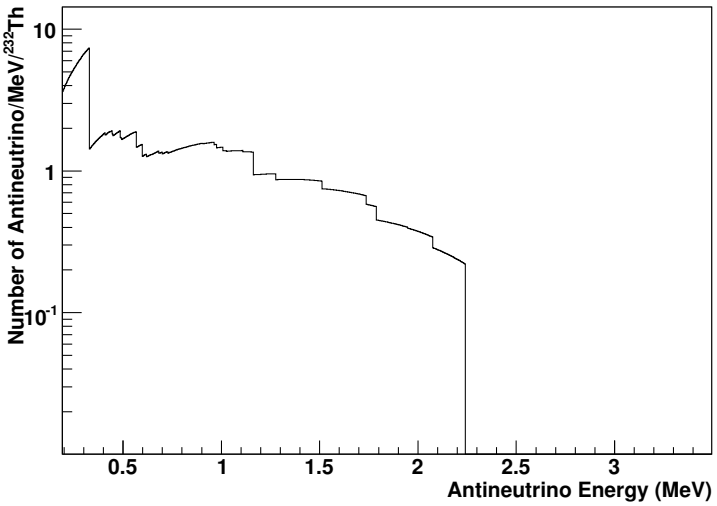

Figure 2.6: The $\bar{\nu}_e$ spectrum of Th chain

2.4 $\bar{\nu}_e$ Propagation in the Earth

2.4.1 Neutrino Oscillations in Matter

The phenomenon of neutrino oscillations has been established by experiments [1][2][7] [8]. When neutrinos propagate, the probability for detecting the neutrino flavour

changes with distance of propagation — it oscillates. The formulism for neutrino oscillations will not be described here; for a review see [9]. Neutrinos propagating through dense matter can have the additional MSW effect, modifying the normal survival probability. The survival probability of an electron neutrino propagating through a uniform medium is [9]:

$$P_{ee} = 1 - \frac{1}{2}\sin^2 2\theta_m (1 - \cos\frac{2\pi|\vec{r_o} - \vec{r}|}{\lambda_m}) \tag{2.9}$$

where

$$\lambda_m = \frac{4\pi E\hbar c}{\Delta M_{21}} \tag{2.10}$$

$$\sin 2\theta_m = \frac{\Delta m_{21}\sin 2\theta}{\Delta M_{21}} \tag{2.11}$$

In Equation 2.10 and 2.11,

$$\Delta M_{21} = \sqrt{\Delta^2 m_{21} + A^2 - 2A\Delta m_{21}\cos(2\theta)} \tag{2.12}$$

where

$$A = 2\sqrt{2}G_F N_e E = 2\sqrt{2}G_F(Y_e/m_n)\rho E \tag{2.13}$$

θ is the oscillation mixing angle and Δm_{21} is the mass-squared difference, $\Delta m_{21} = m_2^2 - m_1^2$. G_F is the Fermi constant, ρ is the mass density of the medium, Y_e the number of electrons per nucleon and m_n is the mass of a nucleon. The relevant neutrino oscillation parameters were measured by SNO and other experiments. The best-fit values of the parameters are [2]

$\Delta m_{21} = 8.0^{+0.6}_{-0.4} \times 10^{-5} eV^2$

$\theta = 33.9^{+2.4}_{-2.2}$ degrees.

2.4.2 $\bar{\nu}_e$ Propagation in the Earth

Equation 2.9 can also be written in a different form

$$P_{ee} = [1 - \frac{1}{2}\sin^2 2\theta_m] + \frac{1}{2}\sin^2 2\theta_m \cos\frac{2\pi|\vec{r_o} - \vec{r}|}{\lambda_m} \tag{2.14}$$

For a neutrino with a given energy, in a medium with fixed electron density, the first term is constant while the second term oscillates. The significance of the two terms when examining a distribution of neutrino sources depends on the distance. If the neutrino source is distributed within a distance of a few times λ_m, the second term will be significant. On the other hand if the source extends to a volume which is many times λ_m, the second term averages to zero and the survival probability can be written approximately as:

$$\bar{P}_{ee} = 1 - \frac{1}{2}\sin^2 2\theta_m \tag{2.15}$$

and an integration over a distribution of sources is greatly simplified.

In the case of geoneutrino calculations, it is very inconvenient to discuss the significance of the two terms in Equation 2.14 in spherical coordinates, so we will discuss it in a simplified, one-dimensional coordinate system. The axis of the new system is the distance from the source to SNOLAB (or any other site being examined).

For an $\bar{\nu}$ with a given energy between 1.8 MeV and 3.2 MeV, going through the Earth with a density between 2.6 g/cm^3 and 13 g/cm^3, according to equation 2.13

$$3.57 \times 10^{-7} eV^2 < A < 3.18 \times 10^{-6} eV^2 \tag{2.16}$$

or

$$0.0045\Delta m_{21} < A < 0.040\Delta m_{21}. \tag{2.17}$$

According to equation 2.12

$$\Delta M_{21} = (0.992 \pm 0.006)\Delta m_{21} \tag{2.18}$$

and then

$$\lambda_m = \frac{4\pi E\hbar c}{\Delta M_{21}} = \frac{1}{0.992 \pm 0.006}\frac{4\pi E\hbar c}{\Delta m_{21}} = (1.008 \pm 0.006)\lambda_o \tag{2.19}$$

For energies in the range we are concerned with, the oscillation wavelength varies by less than 0.6% when the electron density changes from that in the crust to that in the mantle or the core. The oscillation wavelength range of a $\bar{\nu}$ from 1.8 MeV to 3.2 MeV is from 56 km to 103 km, according to equation 2.10 and 2.19.

For distances greater than a few hundred kilometers, if we assume that the Earth is uniform in electron density, it will introduce negligible difference when we discuss the oscillation term. In this case, the survival probability $P_{ee}(\theta, \phi, r, E)$ in the original coordinate system can be written as $P_{ee}(l, E)$ in the new one-dimensional system, where $l = |\vec{r_o} - \vec{r}|$. The source distribution function $S(\theta, \phi, r)$ can be integrated and transfered into a one-dimension function $S(l)$. In this coordinate system, the $\bar{\nu}_e$ flux is

$$\begin{aligned} f(E) &= \int_0^{2R_{earth}} \frac{1}{4\pi l^2}\Phi(E)S(l)P_{ee}(l, E)dl \\ &= \frac{1}{4\pi}[1 - \frac{1}{2}\sin^2 2\theta_m]\Phi(E)\int_0^{2R_{earth}} \frac{S(l)}{l^2}dl \\ &\quad + \frac{1}{8\pi}\sin^2 2\theta_m\Phi(E)\int_0^{2R_{earth}} \frac{1}{l^2}\cos\frac{2\pi l}{\lambda_m(E)}S(l)dl \end{aligned} \tag{2.20}$$

where $\lambda_m(E)$ is the oscillation wavelength of the $\bar{\nu}_e$ with energy E. The $\bar{\nu}_e$ flux is

$$
\begin{aligned}
f &= \int_0^{E_{max}} \Phi(E) \int_0^{2R_{earth}} \frac{1}{4\pi l^2} S(l) P_{ee}(l,E) dE dl \\
&= \frac{1}{4\pi}[1 - \frac{1}{2}\sin^2(2\theta_m)] \int_0^{E_{max}} \Phi(E) \int_0^{2R_{earth}} \frac{S(l)}{l^2} dl \\
&\quad + \frac{1}{8\pi}\sin^2(2\theta_m) \int_0^{E_{max}} \Phi(E) \int_0^{2R_{earth}} \frac{1}{l^2} \cos(\frac{2\pi l}{\lambda_m(E)}) S(l) dE dl
\end{aligned} \tag{2.21}
$$

If we can do the integral of each term in Equation 2.20 and compare them, we can learn the significance of the two terms in a geoneutrino flux calculation.

We can define a ratio as follows

$$
\text{ratio} = \frac{\frac{1}{8\pi}\sin^2 2\theta_{\mathrm{m}} \Phi(\mathrm{E}) \int_0^{\mathrm{R}} \frac{1}{\mathrm{l}^2} \cos\frac{2\pi \mathrm{l}}{\lambda_{\mathrm{m}}(\mathrm{E})} \mathrm{S(l)dl}}{\frac{1}{4\pi}[1 - \frac{1}{2}\sin^2 2\theta_{\mathrm{m}}] \Phi(\mathrm{E}) \int_0^{\mathrm{R}} \frac{\mathrm{S(l)}}{\mathrm{l}^2} \mathrm{dl}} \tag{2.22}
$$

where the numerator in this definition is the second term of Equation 2.20 and the denominator is the first term if $R = 2R_{earth}$. This ratio approximately shows the relative error in the calculation if we take Equation 2.15 as the averaged $\bar{\nu}_e$ survival probability.

The Canadian Shield has fairly uniform thickness within 500 kilometers around SNOLAB, and the thickness t is about 45 kilometers. Because the scale of 500 kilometers is much less than the scale of an Earth radius, we assume the crust in this area to be flat, for the following calculation. In additional, in order to simplify the calculation, we also assume the $\bar{\nu}$ source distribution is uniform in the crust, and also in the mantle. In this case, the one-dimensional U and Th distribution within 500 kilometers around SNOLAB is approximately

$$
S_{U,Th}(l) = 2\pi l^2 \rho_{crust} C^c_{U,Th} \tag{2.23}
$$

when $0 < l < t$ and if $t \leq l \leq 500$ kilometers,

$$S_{U,Th}(l) = 2\pi l t \rho_{crust} C^{c}_{U,Th} + 2\pi l(l-t)\rho_{mantle} C^{m}_{U,Th} \tag{2.24}$$

where ρ_{crust} is the mass density of the crust, ρ_{mantle} is the mass density of the mantle, $C^{c}_{U,Th}$ is the concentration of U or Th in the crust and $C^{m}_{U,Th}$ is the concentration of U or Th in the mantle.

According to this distribution, we calculated the ratio expressed in equation 2.22 within 500 kilometers around SNOLAB and plotted Figure 2.7. The energy of $\bar{\nu}_e$ in the calculation is 2 MeV, as an example within the range 1.8-3.2 MeV. Figure 2.7 shows that the ratio drops quickly first and then oscillates near 0. The final range of the ratio oscillation falls between $\pm 1\%$, which shows that the error will be less than 1% if we use just the averaged survival probability in the geoneutrino spectrum and flux calculation, because we are integrating over distances larger than the oscillation wavelengths.

Figure 2.7 used a very simplified source distribution to estimate the size of the effect of matter oscillations. If in the true source distribution the sources within 50 km completely dominated in their contribution to the total flux, the above calculation which integrated the simplified distribution out to 500 km would not give a correct answer. But, that is not the case. To validate this, the contribution to the total geoneutrino flux for the whole Earth was studied (without including oscillations). Figure 2.8 shows the integrated fraction compared to the total flux as a function of the range from SNOLAB. The result shown in this figure was integrated numerically based on the Earth reference and U and Th distributions shown in the previous sections. Oscillations were not taken into account in this calculation. In other words, here the source distribution was realistic but no oscillations were included while for Figure 2.7 the source distributions were simplified to allow the calculation of the effect from oscillations. When compared they allow us to draw conclusions. From Figure 2.8, we see that integrating out to 500 km distance contains $\sim 60\%$ of the total

contribution to the flux and that sources very near (within 50 km) do not dominate completely. It is clear for distances greater than 500 km, for the oscillation lengths between 56 and 103 km shown previously, taking the averaged survival probability is a valid approximation.

The averaged survival probability of a $\bar{\nu}_e$ within the energy range of 1.8 MeV $\sim$ 3.2 MeV propagating through Earth is

$$\bar{P}_{ee} = 1 - \frac{1}{2}\sin^2 2\theta_m = 1 - \frac{1}{2}(\frac{\Delta m_{21}}{\Delta M_{21}})^2 \sin^2 2\theta \simeq 0.57 \tag{2.25}$$

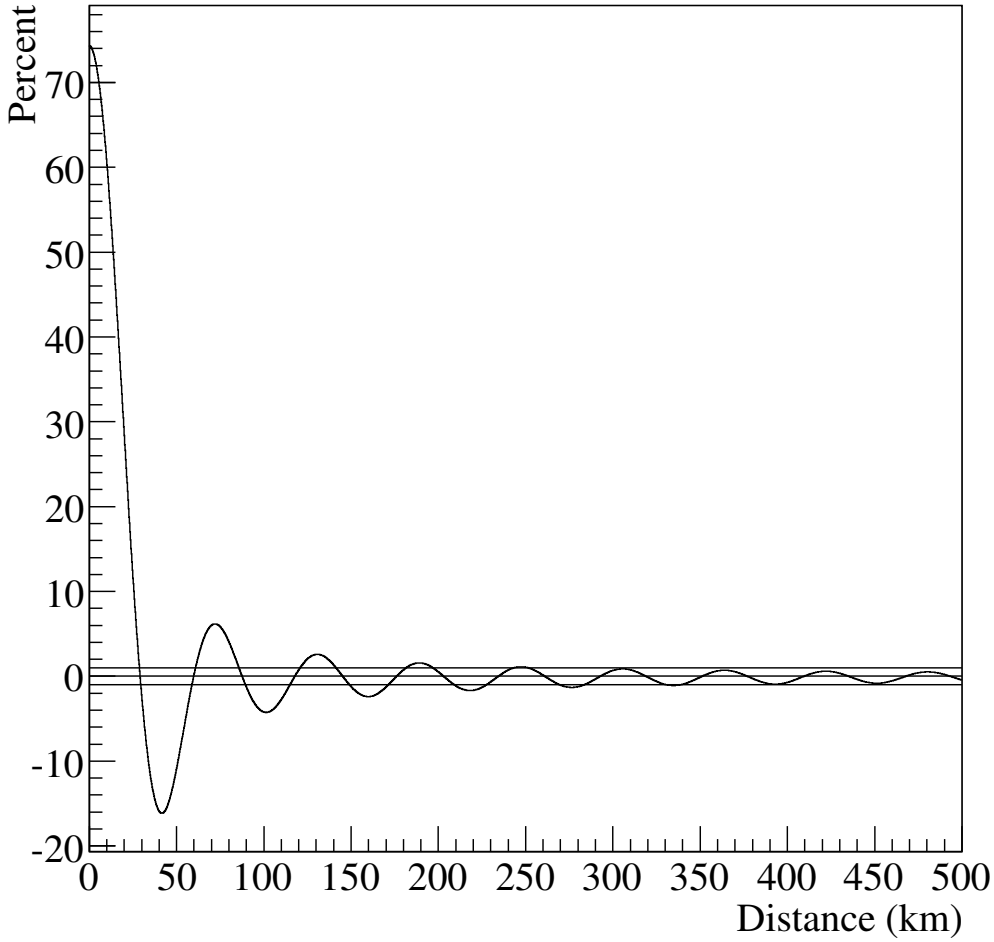

Figure 2.7: The relative error caused by taking the averaged survival probability

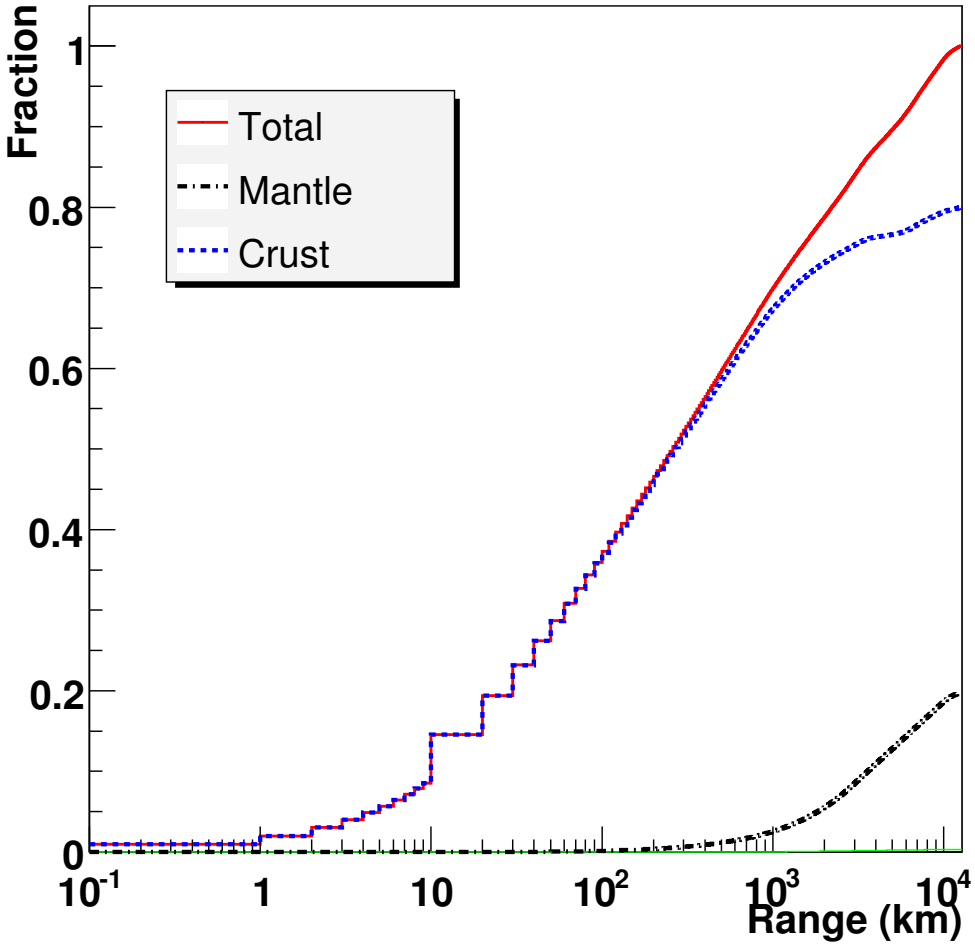

Figure 2.8: The contribution to the geoneutrino flux as a function of the range from SNOLAB

2.5 Geoneutrino Flux and Spectrum at SNOLAB

We have discussed the distribution of geoneutrino sources, ^{238}U and ^{232}Th, in section 2.2, the $\bar{\nu}_e$ spectrum of the two chains in section 2.3 and the propagation in section 2.4. Now we can numerically calculate the geoneutrino spectrum and flux at SNOLAB using Equation 2.3 and Equation 2.4.

The averaged survival probability of a geoneutrino depends very little on energy and can be used for the whole spectrum without introducing significant error in the flux and spectrum calculation. As discussed in the previous section, it can be expressed by

$$P_{ee}(\theta, \phi, r, E) = 0.57 \tag{2.26}$$

Because all the factors except $\Phi(E)$ in Equation 2.3 are independent of the $\bar{\nu}_e$ energy E, the energy spectrum of $\bar{\nu}_e$ at SNOLAB

$$f(E) \propto \Phi(E) \tag{2.27}$$

Table 2.2 gives the concentration of ^{238}U and ^{232}Th in different parts of the Earth. The Earth model Crust 2.0 and the PREM give the mass distribution of the Earth. The ^{238}U and ^{232}Th distribution function $S(\theta, \phi, r)$ can be built numerically from Table 2.2, Crust 2.0 and the PREM.

Associating these factors, we integrated the geoneutrino flux according to Equation 2.4. Table 2.3 shows the results. For comparison, the values assuming that there are no oscillations are also shown.

Table 2.3: The geoneutrino flux at labs.

		^{238}U (10^6cm^{-2}s^{-1})		^{232}Th (10^6cm^{-2}s^{-1})	
		$\times Pee = 1$	$\times Pee = 0.57$	$\times Pee = 1$	$\times Pee = 0.57$
SNOLAB	From Crust	4.14	2.36	3.49	1.99
(46.5N, 81.2W)	Sediment	0.10	0.06	0.08	0.05
Gran Sasso	From Crust	2.05	1.17	1.71	0.97
(42N, 14E)	Sediment	0.41	0.23	0.35	0.20
KamLAND	From Crust	2.30	1.31	1.93	1.10
(36N, 137E)	Sediment	0.18	0.11	0.16	0.09
Central Australia	From Crust	3.40	1.94	2.87	1.64
(25S, 133E)	Sediment	2.36	1.35	1.96	1.12
Himalayas	From Crust	6.03	3.44	5.09	2.90
(33N, 85E)	Sediment	0.10	0.06	0.09	0.05
Hawaii	From Crust	0.28	0.16	0.22	0.12
(20N, 156W)	Sediment	0.03	0.02	0.03	0.02
All sites	From Mantle	1.06	0.60	0.93	0.53

2.6 $\bar{\nu}_e$ From Nuclear Plants

Apart from the natural β^- decays, there are man-made β^- decays on Earth. They are β^- decays of fission products in nuclear power plants. Large amounts of $\bar{\nu}_e$s are produced in nuclear power plants all over the world and become the most significant background for geoneutrino detection. Unlike other backgrounds from outside the detector, they cannot be shielded.

Assuming the $\bar{\nu}_e$ yield of nuclear plants is 5×10^{20} per 2800 MW thermal power [6] and a typical efficiency of 33% for electric/thermal power, the $\bar{\nu}_e$ flux at SNOLAB is

$$f_{n.p.} = \sum_{plants} \frac{1}{4\pi|\vec{r_o} - \vec{r}|^2} \times 5.0 \times 10^{20} \times P/(2.8GW \times 33\%) \qquad (2.28)$$

where $|\vec{r_o} - \vec{r}|$ is the distance from a plant to the lab, P is the electric power of the plant with a unit of GW.

Data for the world's nuclear power plants, including the electric power and loca-

tions, are available at the International Nuclear Safety Center web site operated by Argonne National Laboratory for the US Department of Energy [38]. Some newer data, for example, the exact locations of the nuclear plants, can be found at Nuke Database System created at the Nuclear Training Centre, Ljubljana, Slovenia[39]. With these data we can calculate the total $\bar{\nu}_e$ flux at SNOLAB and other sites from the world's nuclear plants, shown in Table 2.4.

Table 2.4: The $\bar{\nu}_e$ flux at labs from nuclear plants

Sites	Flux (10^6cm^{-2}s^{-1})	
	$\times Pee = 1$	$\times Pee = 0.57$
SNOLAB(46.5N, 81.2W)	1.00	0.57
Gran Sasso(42N, 14E)	0.59	0.34
KamLAND(36N, 137E)	4.20	2.39
Central Australia(25S, 133E)	0.02	0.01
Himalayas(33N, 85E)	0.06	0.03
Hawaii(20N, 156W)	0.03	0.01

The energy spectrum of $\bar{\nu}_e$ from nuclear plants changes over time because the fission rate for each fissile isotope is different. The four significant fissile isotopes in nuclear power plants are ^{235}U, ^{238}U, ^{239}Pu, and ^{241}Pu. As an example, the relative contributions to the number of fissions from the four relevant isotopes as a function of days of reactor at full power in the Gösgen nuclear power plant are shown in Figure 2.9 [6]. Averaged over live time, the relative fission yields from the four fuel components in a typical nuclear power plant are [7]

$$^{235}U : {}^{238}U : {}^{239}Pu : {}^{241}Pu = 0.568 : 0.078 : 0.297 : 0.057 \tag{2.29}$$

The $\bar{\nu}_e$ spectrum of the four fissile isotopes are shown in Figure 2.10 and the time averaged $\bar{\nu}_e$ spectrum of a nuclear reactor is also shown.

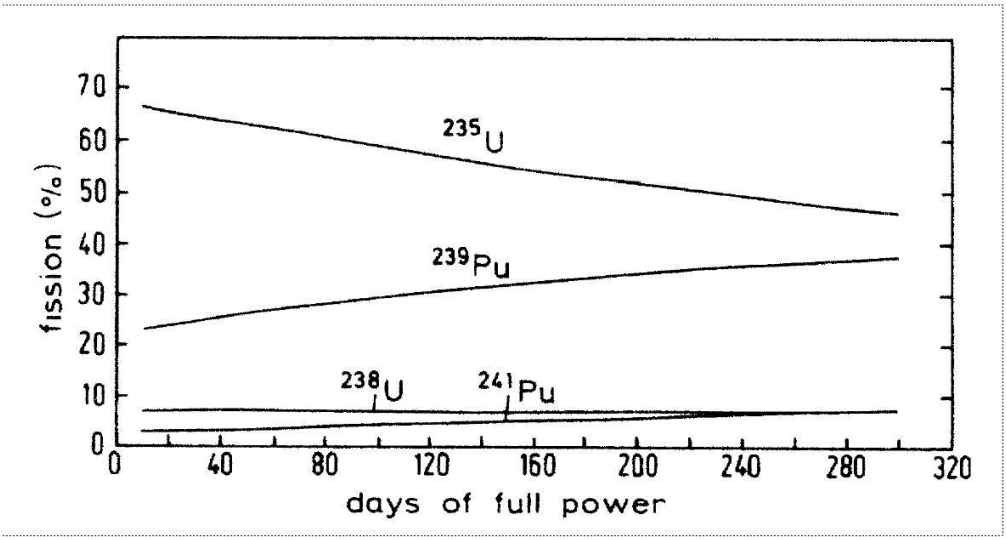

Figure 2.9: Relative contributions to the number of fissions from the four relevant isotopes as a function of days of reactor at full power at the Gösgen reactor [6]

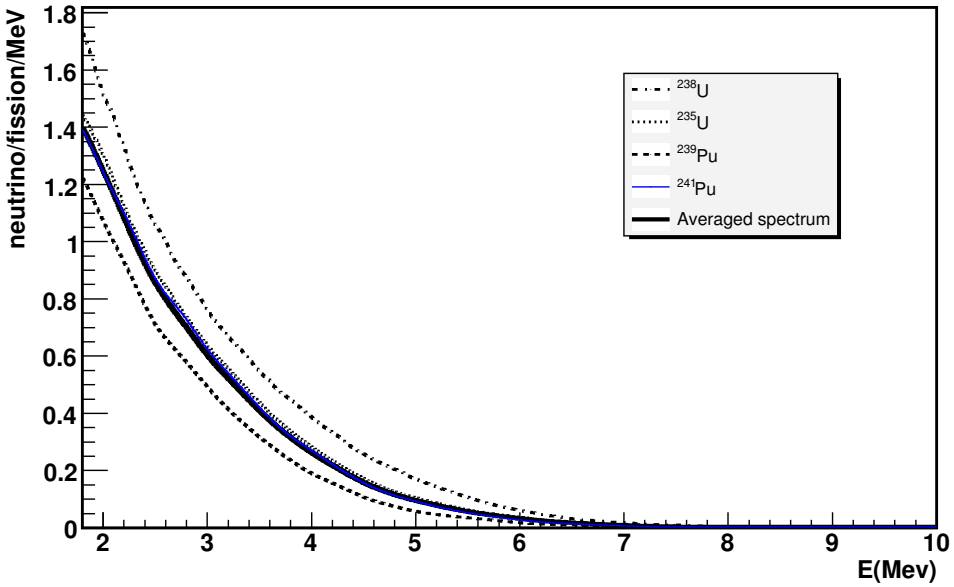

Figure 2.10: $\bar{\nu}_e$ spectrum of the four isotopes and the time averaged $\bar{\nu}_e$ spectrum of nuclear plants [40]

2.7 $\bar{\nu}_e$ Events in the SNO+ Detector

When the geoneutrinos and $\bar{\nu}_e$s from reactors arrive at the SNO+ detector, some of them will take part in the inverse β reaction; that is how they will be detected. The cross section of this reaction is extremely small and can be expressed to the lowest-order by the following equation (if neglecting the neutron recoil)[41][25]

$$\sigma(E_\nu) = \frac{2\pi^2\hbar^3}{m_e^5 c^8 f\tau_n}(E_\nu - \Delta Mc^2)[(E_\nu - \Delta Mc^2)^2 - (m_e c^2)^2]^{1/2} \qquad (2.30)$$

where ΔM is the neutron-proton mass difference and the $f\tau_n$ values come from neutron β decay [42]. Multiplying this cross-section by the geoneutrino spectra and the proton number assumed in SNO+, we get the energy spectra of the geoneutrino events, shown in Figure 2.11. Similarly, the energy spectrum of $\bar{\nu}_e$ events from reactors can also be calculated and is shown in Figure 2.11.

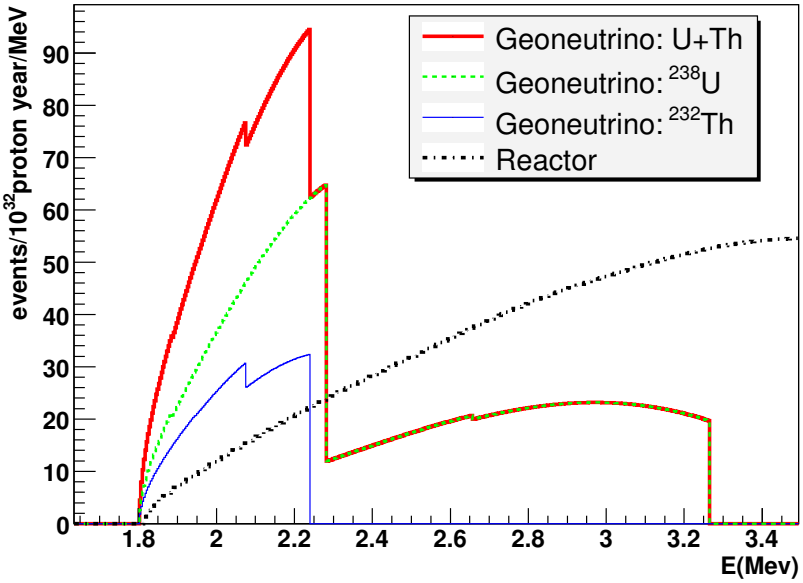

Figure 2.11: Geoneutrino and reactor $\bar{\nu}_e$ event spectrum at SNO+

The integrated geoneutrino event spectrum and integrated reactor $\bar{\nu}_e$ event spectrum at SNO+ are shown in Figure 2.12. The total geoneutrino event rate at SNO+

is 49 events/10^{32} proton-years including an average survival probability of 0.57 due to oscillations. The reactor $\bar{\nu}_e$ event rate within the geoneutrino event energy range ($\leq$3.3 MeV) is about 44 events/10^{32} proton-years while the total reactor $\bar{\nu}_e$ event rate is 177 events/10^{32} proton-year, assuming the same average survival probability.

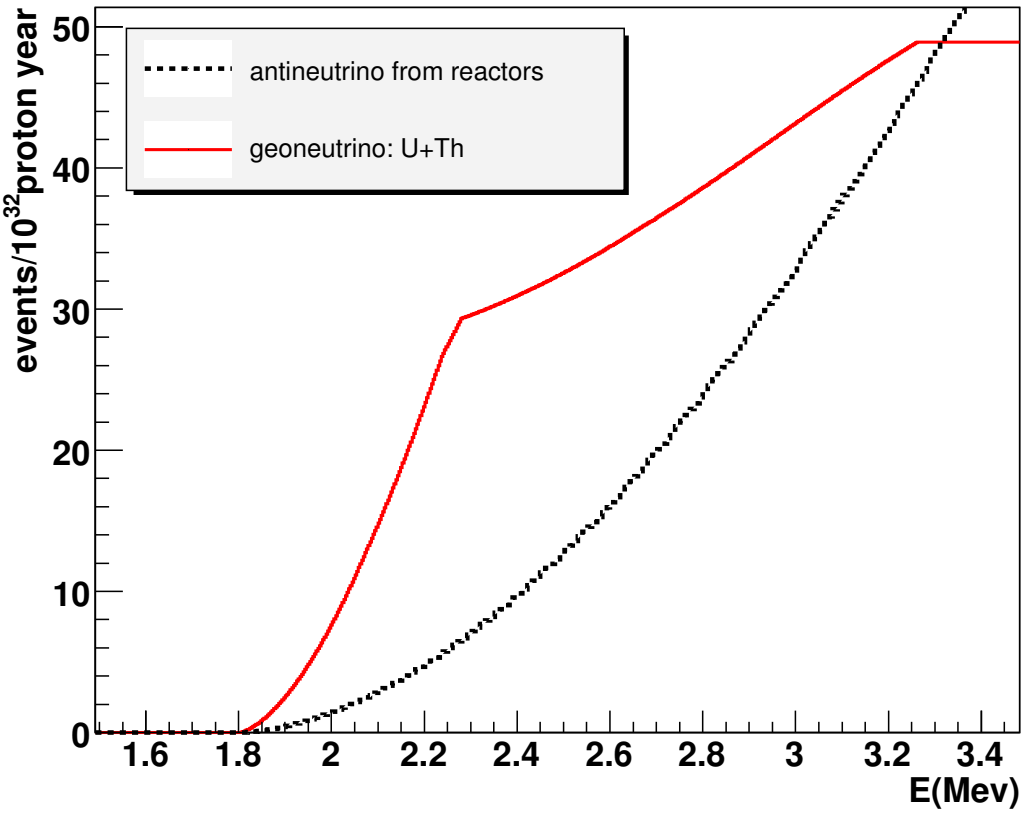

Figure 2.12: Integrated geoneutrino and reactor $\bar{\nu}_e$ event spectrum at SNO+

2.8 Summary of Geoneutrino Physics at SNO+

This chapter described a reference model of the Earth used to calculate the flux and spectrum of geoneutrinos. Because the deepest bore hole made in the Earth is only ∼10000 meters deep, most of the structural information of the model is revealed by seismological analysis and geochemical information is extracted from indirect analysis. There are many assumptions in the model and uncertainties are large. Fortunately, SNOLAB is located in the Canadian Shield, which is the best studied area of crust on the Earth. The continental crust is fairly uniform around SNOLAB and according to Figure 2.8, the first 500km around SNOLAB contribute about 60% to the total geoneutrino flux. The geoneutrino event rate at SNO+ is expected to be 49 events/10^{32} proton-years for 100% detection efficiency.

As a significant background, the $\bar{\nu}_e$ from the nuclear plants were also studied. The event rate of nuclear plant $\bar{\nu}_e$ events within the energy range of geoneutrinos is 44 events/10^{32} proton-years. The energy spectrum of the nuclear plant events are well understood and the whole spectrum can be fitted according to the higher energy part allowing some separation from the geoneutrino events.

Chapter 3. BACKGROUNDS AND LIQUID SCINTILLATOR PURIFICATION

3.1 Backgrounds in SNO+

The SNO+ detector detects neutrinos by observing the scintillation photons produced by the scattered electrons of the neutrino-electron elastic scattering reaction. All other processes which produce scintillation photons are backgrounds for neutrino detection. It detects antineutrinos by a delayed coincidence between scintillation produced by a positron followed by a neutron capture. All other processes which produce similar delayed coincidences are backgrounds for antineutrino detection.

3.1.1 Backgrounds for Neutrino Detection

α, β, γ decays inside the detector are backgrounds for neutrino detection. The energetic electrons produced by β decays can produce scintillation photons and form a signal similar to neutrino events. γ rays can scatter electrons by Compton scattering and then produce scintillation light. High energy α particles produced from α decays can also produce scintillation light. These can be differentiated from electrons by looking at the time profile of light emission, called pulse shape discrimination.

To reduce the background, the detector must be built with materials which have extremely low radioactive impurities. The liquid scintillator must be purified to reduce radioactive impurities to acceptable levels. The target levels of the impurities in SNO+ are being set according to the physics goals, determined by simulations.

As a reference for the discussion here, Table 1 shows the relevant naturally existing radioactive background isotopes, the levels achieved and the target levels in the liquid scintillator of KamLAND, a similar experiment to SNO+.

The backgrounds in KamLAND corresponding to the achieved impurity levels in Table 3.1 are shown in Figure 3.1. It shows that ^{210}Bi, ^{210}Po, the short-lived daughters of ^{210}Pb, and ^{85}Kr are the dominant background sources for the detections of ^{7}Be neutrinos and pep neutrinos. The background caused by them must be reduced 5 or 6 orders of magnitude. KamLAND has the goal to reach background levels shown in Figure 3.2, corresponding to the target levels given in Table 3.1.

Table 3.1: Radioisotopes and the levels achieved at KamLAND

Isotope	*Half-life*	*Concentration Achieved*(g/g)	*Target Level*(g/g)
^{39}Ar	$269y$	$0.2Bq/m^3$	$1\mu Bq/m^3$ [43]
^{40}K	$1.26 \times 10^9 y$	$\leq 2.7 \times 10^{-16}$	10^{-17} [43]
^{85}Kr	$10.7y$	$0.46Bq$	$10^{-6}Bq$ [43]
^{210}Pb	$22.3y$	$\sim 10^{-20}$	5×10^{-25} [43]
^{232}Th	$1.4 \times 10^{10} y$	5.2×10^{-17}	10^{-17} [7]
^{238}U	$4.46 \times 10^9 y$	3.4×10^{-18}	10^{-18} [7]

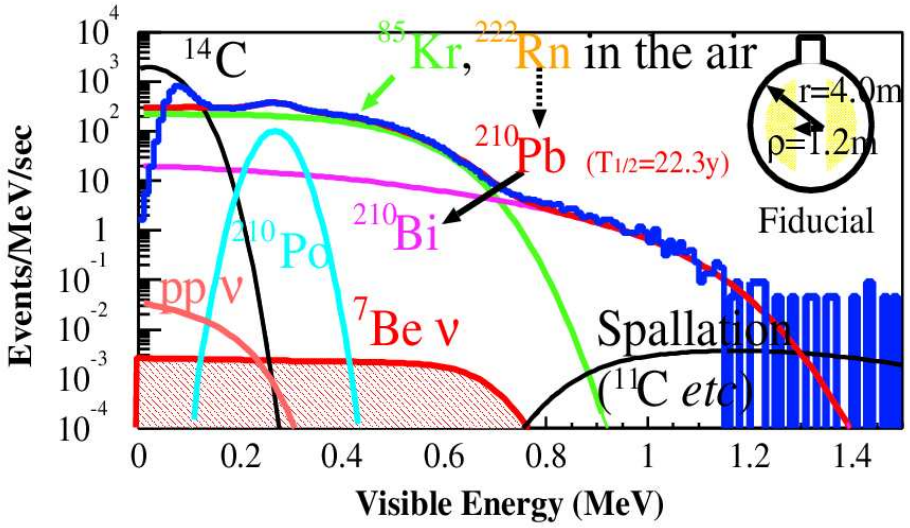

Figure 3.1: Backgrounds achieved in KamLAND [43]

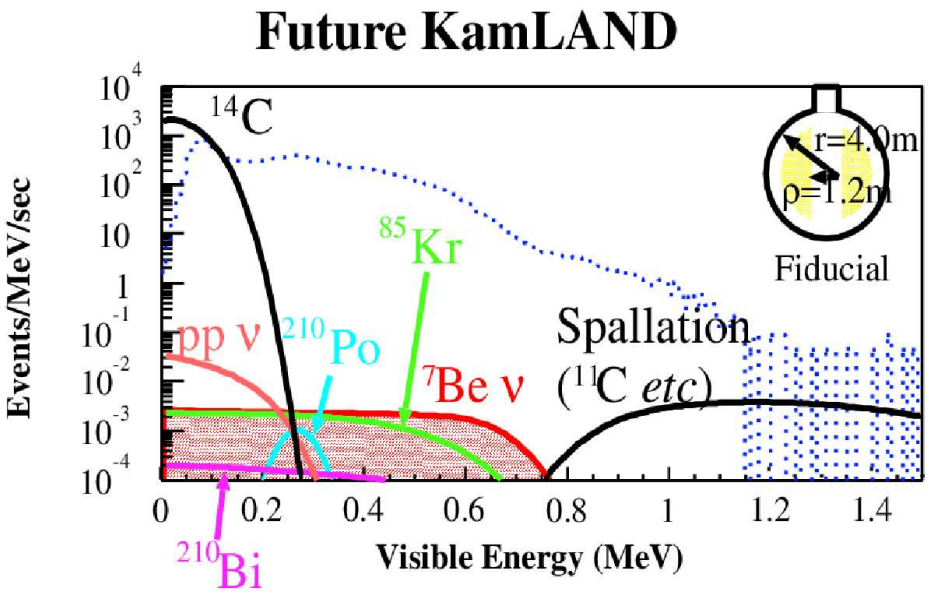

Figure 3.2: Objective background levels in KamLAND [43]

^{210}Pb is a daughter of $^{222}_{86}$Rn, a gas produced in the ^{238}U decay chain. The half life of $^{222}_{86}$Rn is 3.82 days. Unfortunately, $^{222}_{86}$Rn is highly soluble in organics including the liquid scintillator in SNO+. It's believed that the ^{210}Pb in the KamLAND liquid scintillator originated from radon exposure. The concentration of radon is very high in the air of underground labs because the concentration of ^{238}U in rocks is high. If there is unintended introduction or diffusion of underground air in the liquid scintillator, then ^{210}Pb, the daughter of $^{222}_{86}$Rn, will accumulate in the detector and contaminate it. It is vital to avoid the contamination from this radioactive gas. To achieve that, the detector must be sealed, handling of the liquid scintillator must avoid contact with air, and the air in labs ideally would be radon reduced.

In addition to the radioactive backgrounds originating within the detector, there are backgrounds from outside the detector. Although the SNO detector used materials which have very low radioactive impurities, it is still important to understand

these backgrounds. Compared to detector materials, the rock walls in the lab have much higher concentrations of radioactive isotopes and there is no way to remove them. These radiations are attenuated by the light water around the detector used as shielding. The SNO detector was suitably designed to reduce these γ rays. External γ backgrounds are further reduced by making a fiducial volume cut, accepting events only within a limited radius from the center.

The cosmogenic isotopes produced by muons and their secondary shower particles are also potential background sources. Fortunately, SNO+ is so deep that the muon rate in SNO+ is very low ($\sim$ 400 times lower than in KamLAND) and the isotopes produced by these particles are very rare. Thus this background is not significant in SNO+.

This survey of potential backgrounds highlights the most important one ^{210}Pb. ^{210}Pb contamination can also produce a background for antineutrino detection.

3.1.2 Backgrounds for Antineutrino Detection

The SNO+ detector detects antineutrinos via this reaction,

$$\bar{\nu}_e + p \longrightarrow e^+ + n \tag{3.1}$$

The signal in the detector is a delayed coincidence between the prompt e^+ event and the delayed γ ray produced by a neutron captured by a proton. This delayed coincidence signal greatly reduces the number of potential backgrounds.

A neutron in the scintillator with a few MeV kinetic energy can produce a similar coincidence. It scatters a proton first, which is the prompt event, and then it can be captured by a nucleus to emit a γ ray as the delayed event. Fast neutrons can look like antineutrinos in the detector.

Possible neutron sources (few MeVs) in the SNO+ detector include (α, n) reactions and cosmogenic radioactive isotopes. According to the experience of Kam-

LAND, the following types of neutron sources are negligible: spontaneous fission and other direct neutron emitters, correlated decays in the radioactive background decay chain, fast neutrons from cosmic ray interactions, (γ, n) reactions and solar ν_e induced break-up of ^2H [27] [44]. The background produced by cosmogenic radioactive isotopes at KamLAND is also not significant. This background in SNO+ will be even lower than that at KamLAND because SNOLAB is much deeper than KamLAND and the muon rate is more than 2 order of magnitude lower than at KamLAND [17]. Therefore, the only significant neutron source in SNO+ is (α, n) reactions.

3.2 (α, n) Fake $\bar{\nu}_e$ Event

For convenience, we call the events caused by an (α, n) neutron "(α, n) fake $\bar{\nu}_e$ event". The fake $\bar{\nu}_e$ event rate depends on the (α, n) neutron yield, spectrum and transport in the liquid scintillator. A method to calculate neutron yields in compounds and mixtures was developed and applied in SNO[45] [46] . The total neutron yield and spectrum can be calculated approximately from the yields and spectrum for individual isotopes. The transport can be simulated using Monte Carlo software packages, such as Geant4.

The thick-target (α, n) neutron productivity $P(E_\alpha, i)$ of an α particle with initial energy E_α reacting with an target isotope i is:

$$P(E_\alpha, i) = \int_0^R n_i \sigma_i dx \tag{3.2}$$

where R, n_i and σ_i are the range of the α particle, the atom number density of the isotope and the (α, n) cross section of isotope respectively. For convenience, we transform the integral to an integration over the energy of the α particles because it is much easier to get the initial energy of the α particles. Then the productivity is:

$$P(E_\alpha, i) = \int_0^{E_\alpha} \frac{n_i \sigma_i}{-dE/dx} dE$$
$$= \int_0^{E_\alpha} \frac{n_i \sigma_i}{S(E)} dE \tag{3.3}$$

where $S(E) = -dE/dx$ is the stopping power of the α particle in the medium as a function of the α energy. The neutron yield from the reaction between isotope i and the α particle with an initial energy E_α is

$$Y(E_\alpha, i) = N_\alpha P(E_\alpha, i)$$
$$= N_\alpha \int_0^{E_\alpha} \frac{n_i \sigma_i}{S(E)} dE \tag{3.4}$$

The total neutron yield is the sum of the yields from all the α particles and all the isotopes:

$$Y = \sum_\alpha \sum_i N_\alpha \int_0^{E_\alpha} \frac{n_i \sigma_i}{S(E)} dE \tag{3.5}$$

According to Equation 3.5, the total number of neutrons produced by (α, n) reactions depends on four factors: (1) the strength and energy of α sources; (2) the densities of target isotopes;(3) the cross sections of the reactions; (4) the stopping power of α particles in the liquid scintillator. These factors will be discussed in detail in the following sections.

3.2.1 The α Particles in SNO+

At this moment, we don't know how low the radioactive background will be in SNO+. Because SNO+ has KamLAND and other experiments as examples and can learn from their experiences, it's reasonable to assume that SNO+ can achieve the same

level as, or lower than, KamLAND's background. For example, SNO+ will try to avoid the contamination of the liquid scintillator by ^{222}Rn. ^{222}Rn is the source of ^{210}Pb accumulated in the KamLAND detector. Table 3.2 shows α background levels achieved in KamLAND as a reference for our detector.

Table 3.2: The α background in KamLAND as a reference for SNO+ [43]

α *Source Isotopes*	*Energy*(MeV)	*Strength*$(Hz/kiloton)$
^{222}Rn	5.49	$\sim 8 \times 10^{-4}$
^{218}Po	6.02	$\sim 8 \times 10^{-4}$
^{214}Po	7.69	$\sim 8 \times 10^{-4}$
^{210}Po	5.3	~ 60
^{232}Th	4.01	$\sim 3 \times 10^{-4}$
^{228}Th	5.423	$\sim 3 \times 10^{-4}$
^{224}Ra	5.685	$\sim 3 \times 10^{-4}$
^{220}Rn	6.288	$\sim 3 \times 10^{-4}$
^{216}Po	6.778	$\sim 3 \times 10^{-4}$
^{212}Bi	6.04	$\sim 3 \times 10^{-4}$
^{212}Po	8.79	$\sim 3 \times 10^{-4}$

From Table 3.2 we find that more than 99.9% of the α particles are produced from ^{210}Po and have an energy of 5.3 MeV. ^{210}Po follows from ^{210}Pb decay; it is KamLAND's significant ^{210}Pb contamination that is noteworthy. The focus of this thesis is understanding this potential background to the $\bar{\nu}_e$ signal.

3.2.2 The Concentrations of Target Isotopes

The liquid scintillator of SNO+ will be a solution consisting of Linear Alkyl Benzene (LAB) and 2,5-diphenyloxazole (PPO). LAB is the solvent and PPO is solute. For each liter of LAB, there will be 2 to 4 grams of PPO dissolved. The chemical formula of PPO is $C_{15}H_{11}NO$. Table 3.3 shows the composition of LAB used in SNO+.

Assuming natural isotopic abundance of the 4 elements in the liquid scintillator, the atom densities of the isotopes were calculated and shown in Table 3.4. The atom number fractions of the isotopes in the liquid scintillator and the (α,n) thresholds

Table 3.3: The composition of LAB

Molecular Equation	Content (mass %)
$C_{16}H_{26}$	20.4
$C_{17}H_{28}$	43.2
$C_{18}H_{30}$	33.4
$C_{19}H_{32}$	1.8
$C_{15}H_{24}$	1.2

are also shown.

Table 3.4: The isotopes in the liquid scintillator(assuming 2g PPO/l)

Isotopes	Atom numbers (l^{-1})	Target Fraction	(α,n) Threshold[MeV]
^{1}H	6.265×10^{25}	0.6227	118.01 [44]
^{2}H	9.399×10^{21}	9.34×10^{-5}	12.52 [44]
^{12}C	3.761×10^{25}	0.3738	11.34 [44]
^{13}C	4.183×10^{23}	0.00416	$\leq$ 0.8 [47]
^{14}N	5.431×10^{21}	5.4×10^{-5}	6.09 [44]
^{15}N	2.017×10^{19}	2.0×10^{-7}	$\sim$ 8 [43]
^{16}O	5.438×10^{21}	5.4×10^{-5}	15.18 [44]
^{17}O	2.180×10^{18}	2.17×10^{-8}	$\leq$ 0.9 [48]
^{18}O	1.090×10^{19}	1.08×10^{-7}	$\leq$ 0.5 [48]

According to the threshold energy shown in the table, the possible targets below 5.3 MeV are ^{13}C, ^{17}O and ^{18}O. The fractions of ^{17}O and ^{18}O are 3 or 4 magnitudes smaller than that of ^{13}C therefore ^{13}C is the main target to be considered.

3.2.3 The Cross Sections of the (α, n) *Reactions*

The cross section of $^{17}\mathrm{O}(\alpha, n)^{20}\mathrm{Ne}$ is shown in Figure 3.3 and cross section of $^{18}\mathrm{O}(\alpha, n)^{21}\mathrm{Ne}$ is shown in Figure 3.4 and Figure 3.5. The cross section of $^{13}\mathrm{C}(\alpha, n)^{16}\mathrm{O}$ is shown in Figure 3.6. The accuracy of the $^{13}\mathrm{C}(\alpha, n)^{16}\mathrm{O}$ cross section is much more important than that of $^{17}\mathrm{O}(\alpha, n)^{20}\mathrm{Ne}$ and $^{18}\mathrm{O}(\alpha, n)^{21}\mathrm{Ne}$ because ^{13}C is the main target, whose density is 3 or 4 orders of magnitude higher than that of ^{17}O and ^{18}O. In the KamLAND paper [27], they applied the cross sections provided by JENDL[49] with an uncertainty of 20%, which is one of the main uncertainty sources of their geoneutrino

estimation. To elevate the accuracy of the background estimation for antineutrino detection, the absolute cross section of this reaction has been measured at E_α from 0.8 to 8 MeV with an overall accuracy of 4% by S. Harissopulos et al. [47]. The numeric Table A.1 in the Appendix of this thesis lists values for the $^{13}C(\alpha, n)^{16}O$ cross section and these values were used to plot Figure 3.6.

3.2.4 The Mass Stopping Power of α Particles

When ions move in a medium, they interact with the electrons and nuclei of the medium and deposit energy into it. The energy deposited per unit length is the stopping power. In the SNO+ detector, the α particles move in the liquid scintillator and lose their energy until a reaction happens or the α particles stop.

According to Bragg's Rule, the stopping power of ions in a compound may be estimated by the linear combination of the stopping powers in individual elemental materials [51]. The α stopping power in a compound or mixture is approximately

$$S(E) = \sum_i \rho_i S_i^m \tag{3.6}$$

where ρ_i is the mass density of element i in the compound or mixture and S_i^m is the mass stopping power of element i. Figure 3.7 shows the mass stopping power of the elements H, C, N and O simulated by the software package SRIM2003 [52] and the mass stopping power of α particles in the liquid scintillator of SNO+ calculated according to Equation 3.6. The stopping power of α particles in the liquid scintillator is shown in Figure 3.8.

Because the uncertainty of the stopping power of α particles in the liquid scintillator is one of the main sources of the neutron yield uncertainty, trying to reduce this uncertainty is a good way to improve the estimation of antineutrino backgrounds. The inaccuracy of Bragg's Rule is caused by the difference between the electron orbits in elemental materials and the electron orbits of the same atoms in compounds.

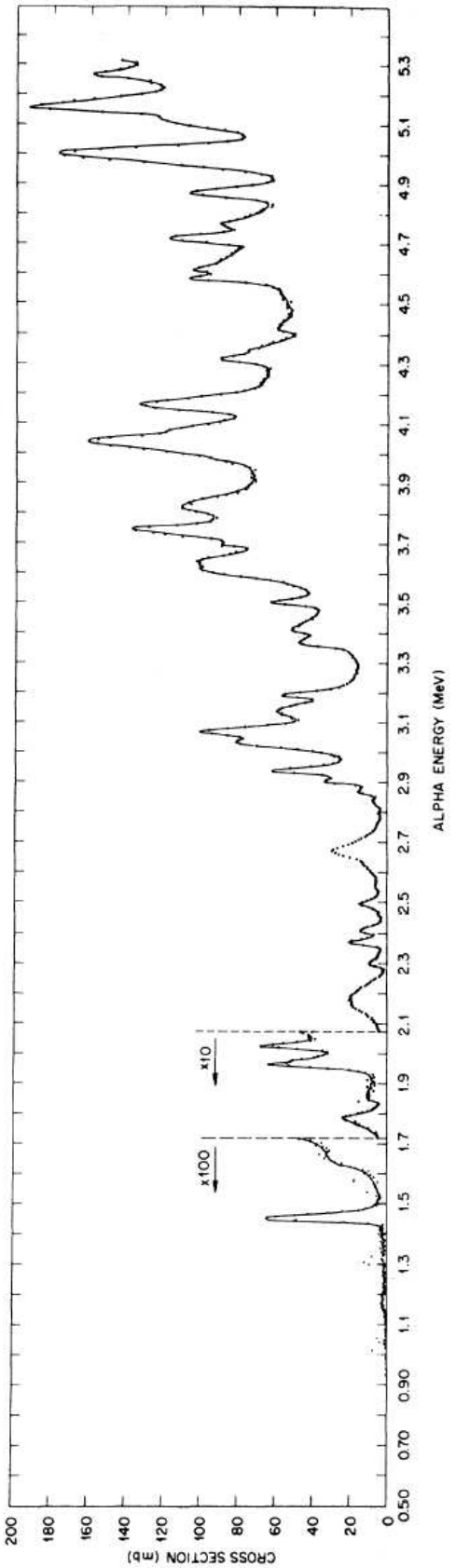

Figure 3.3: Cross section of $^{17}\mathrm{O}(\alpha, n)^{20}\mathrm{Ne}$ [48]

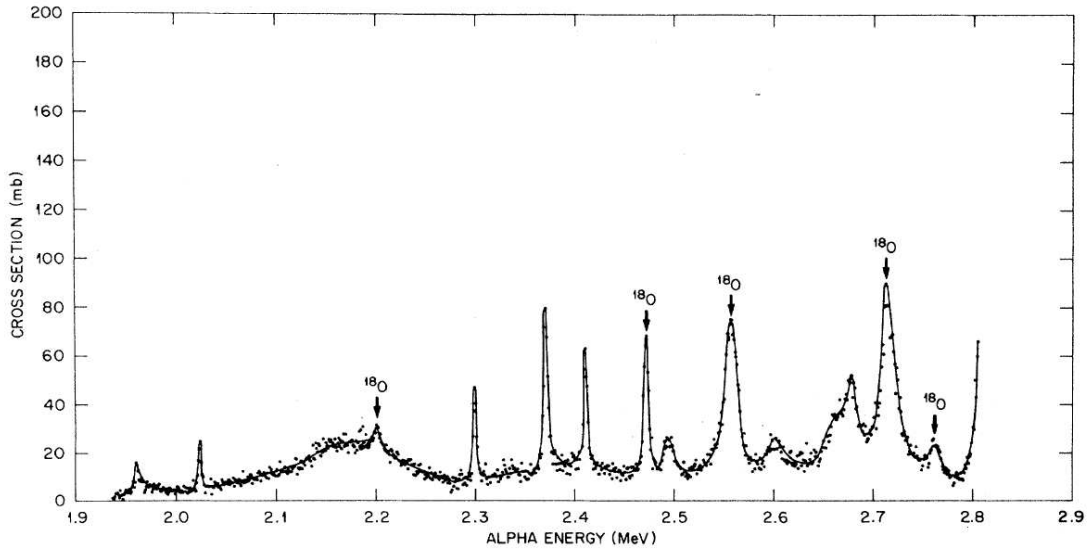

Figure 3.4: Cross section of $^{18}\mathrm{O}(\alpha, n)^{21}\mathrm{Ne}$ [48]

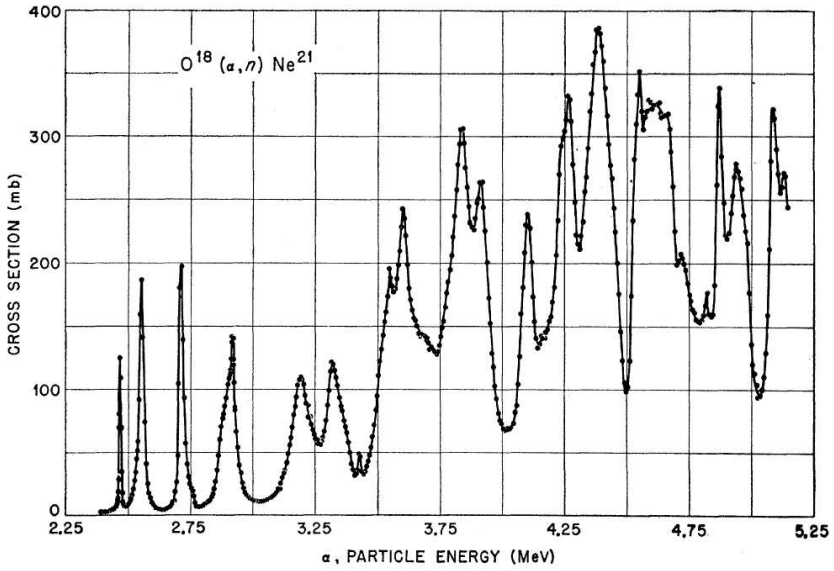

Figure 3.5: Cross section of $^{18}\mathrm{O}(\alpha, n)^{21}\mathrm{Ne}$ [50]

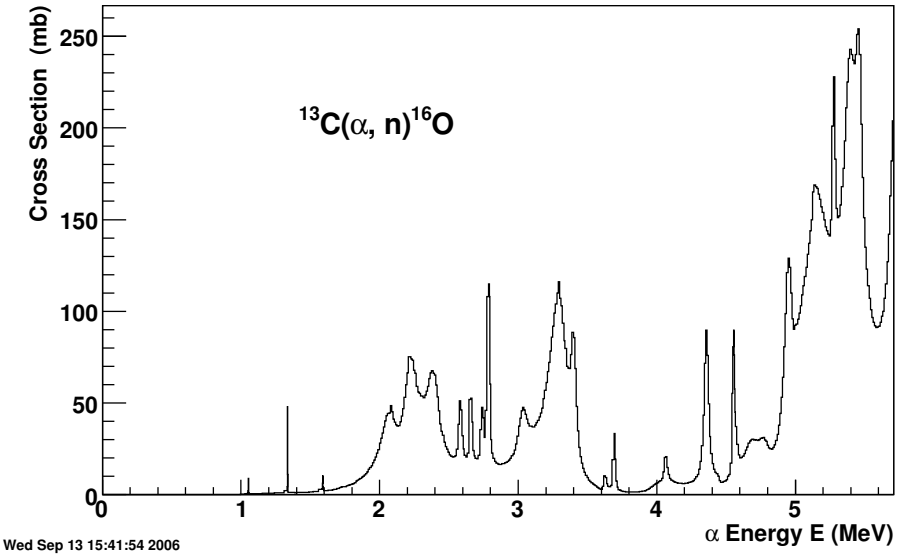

Figure 3.6: Cross section of $^{13}\mathrm{C}(\alpha, n)^{16}\mathrm{O}$

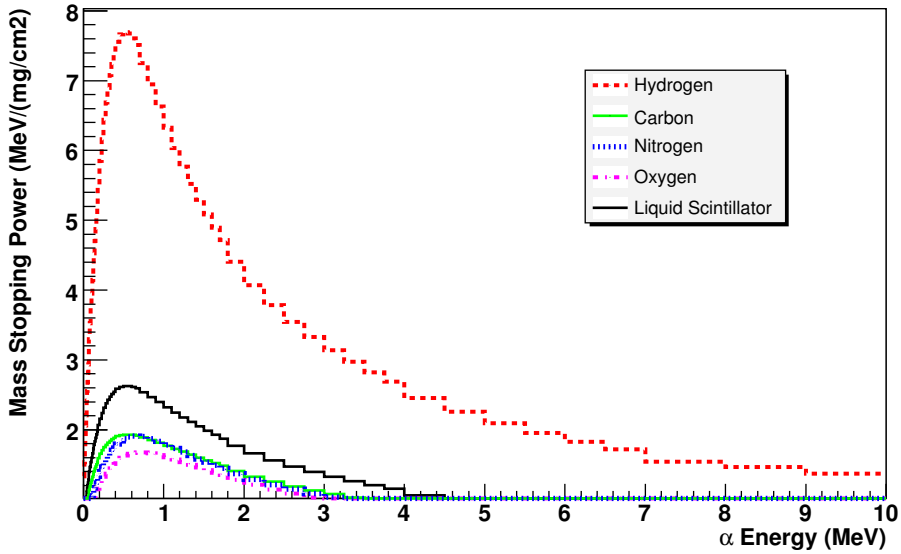

Figure 3.7: The mass stopping power of α particles in liquid scintillator of SNO+ and in the elemental materials of H, C, N, O.

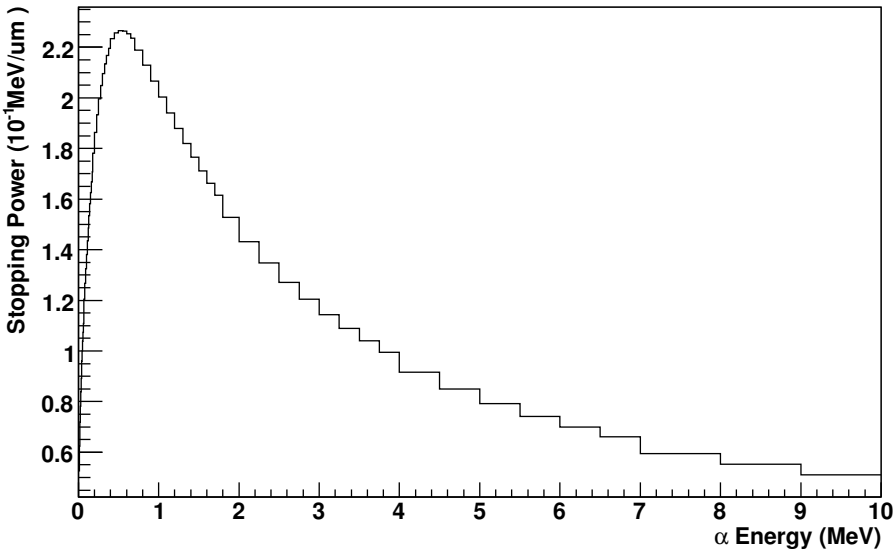

Figure 3.8: The stopping power of α particles in liquid scintillator of SNO+

The energy loss caused by electrons depends on the orbital and excitation structure of the matter. The rule is accurate with reasonable deviation; usually the measured stopping power of an ion in compounds deviates less than 20% from the prediction by Bragg's Rule. One has to either measure the stopping power experimentally or calculate it theoretically with corrections based on Bragg's rule. Hundreds of papers discuss ways to make these corrections. One of the these theoretical methods is the Core and Bond (CAB) approach. It suggests that stopping powers in compounds can be estimated using the superposition of stopping by atomic cores and then adding the stopping power due to the bonding electrons [53]. The core stopping simply follows the Bragg's rule because the atomic cores don't change much when they become part of compound molecules. The necessary stopping corrections are due to the chemical bonds of the compound and can be evaluated depending on the simple chemical nature of the compounds, in our case, the components of the liquid scintillator. This work will use the uncorrected Bragg's rule stopping power calculated for liquid scintillator.

3.2.5 The (α, n) Neutron Yield

According to Equation 3.5 and Equation 3.6, the total neutron yield of (α, n) reactions in the liquid scintillator is

$$Y = \sum_{\alpha} \sum_{i} N_{\alpha} \int_{0}^{E_{\alpha}} \frac{n_i \sigma_i}{\sum_j \rho_j S_j^m} dE \tag{3.7}$$

where α indicates the α sources, i indicates the targets and j indicates the elements in the liquid scintillator. The only significant contribution to the total (α, n) neutron yield is from the reaction $^{13}\mathrm{C}(\alpha, n)^{16}\mathrm{O}$ where the α source is ^{210}Po. Then Equation 3.7 becomes

$$Y = N_{\alpha} \int_{0}^{5.3MeV} \frac{n_{^{13}C} \sigma}{\sum_j \rho_j S_j^m} dE \tag{3.8}$$

By numerically integrating this equation, and using the α strength, the ^{13}C atom density, the cross section and the stopping power shown in the previous sections, we get a neutron yield of 112 neutrons/kiloton-year for a ^{210}Po decay rate of 60 Bq/kiloton.

3.2.6 A Background for Geoneutrinos by (α, n) Neutrons

To estimate the background for geoneutrinos caused by (α, n) neutrons, we have to determine how many of those neutrons will cause the fake $\bar{\nu}_e$ events within the energy range of geoneutrinos to be detected by SNO+ detector. We base this part of our estimation on the work in the PhD thesis of Enomoto[32]. In that thesis, Enomoto estimated the neutron yield in KamLAND to be 64 neutrons/livetime. Because the live time of KamLAND is about 514 days and the fiducial mass is about 408 tons, this neutron yield also equates to 111 neutron/kiloton-year, which is close to our estimation for SNO+.

Figure 3.9 shows the result of Monte-Carlo simulations based on Geant3 for the

KamLAND detector [32]. There are 3 peaks in the simulated spectrum. The one from 0 MeV to 4 MeV is made by protons scattered by neutrons which correspond to the ground state ^{16}O as the product of the $^{13}C(\alpha, n)^{16}O$ reaction. The one from 4 MeV to 5.5 MeV consists of 4.4 MeV γ rays from the reaction $^{12}C(n, n\gamma)^{12}C$ together with scattered protons. The third peak around 6 MeV is made by γ rays or conversion electrons and positrons from the excited ^{16}O as the product of $^{13}C(\alpha, n)^{16}O^*$ reaction. 44 of the 64 events fall into the geoneutrino analysis window. Assuming the same fraction will be in SNO+, then the geoneutrino background caused by (α, n) neutrons in SNO+ will be 78 events/kiloton-year or 106 events/ 10^{32} proton-year.

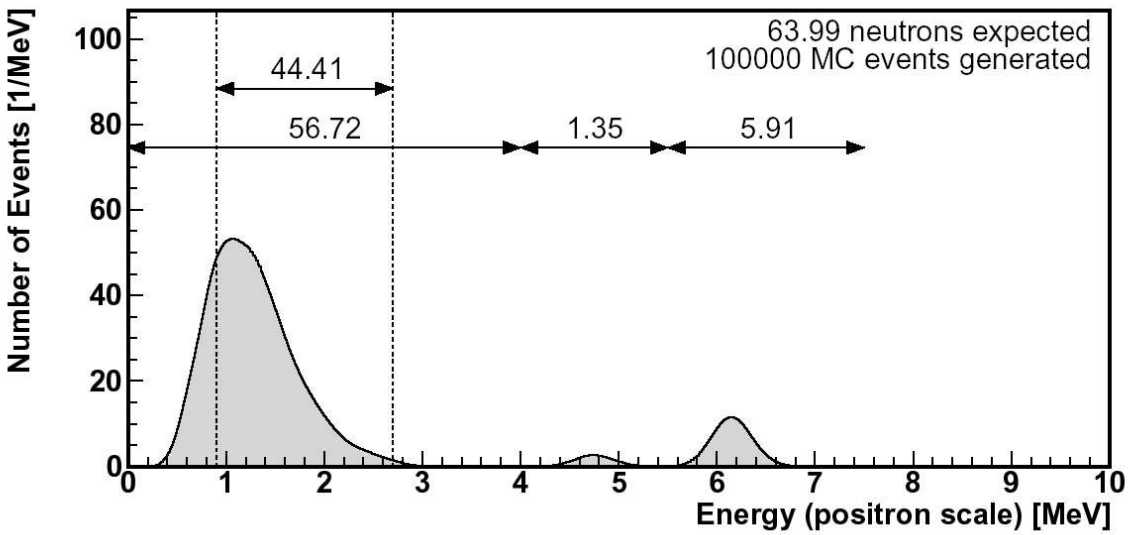

Figure 3.9: Visible energy spectra of $^{13}C(\alpha, n)^{16}O$ by α particles from ^{210}Po [32], with energy resolution of KamLAND

3.3 Purification of Liquid Scintillator by Distillation

To reduce the background, radioactive impurities must be removed from the liquid scintillator (LS). The main radioactive contaminants which may accumulate in the scintillator are ^{39}Ar, ^{40}K, ^{85}Kr, ^{210}Pb, ^{232}Th, ^{238}U. ^{210}Pb is a particular problem

because it accumulates due to radon exposure and thus the entire radon exposure history must be controlled. In this section, I will discuss the removal of ^{210}Pb by distillation. Because ^{40}K, ^{232}Th and ^{238}U are non-volatile elements, distillation can also remove these three isotopes. Removing ^{39}Ar and ^{85}Kr is not included in my discussion and these do not produce backgrounds for antineutrino detection in SNO+.

As discussed previously, ^{210}Pb originates from ^{222}Rn in the air. ^{210}Pb can be accumulated in the liquid scintillator because its half life, which is 22.3 years, is much longer than that of other daughters of ^{222}Rn. The possible chemical form of ^{210}Pb in LS are ionic, metallic and organic. None of these forms can be ignored because the required level of ^{210}Pb in the LS is extremely low. The purification must be very effective for all these three forms.

There are several methods of purification including distillation, adsorption, water extraction and acid extraction. Two factors must be considered when adopting one of these methods: the reduction efficiency of ^{210}Pb and the optical properties of the scintillator after the purification including the light yield and the attenuation length of the LS. Our experiment shows that distillation not only reduces Pb background in LS with high efficiency, but also improves the light attenuation length effectively. This is a merit of distillation. There are also some disadvantages including safety concerns and energy consumption.

Solvent purification by distillation is based on the fact that in a boiling mixture the components having lower boiling points are more likely to vaporize than the components having higher boiling points. Therefore, when this vapour is cooled and condensed, the fraction of the volatile components in the condensate will be higher than that in the original mixture and the mixture left will contain more of the less volatile components than that of the original mixture. The Pb species contained in the LS have much higher boiling points than those of LAB and PPO, therefore they will remain in the residue of LS distillation and then the LS is purified.

One problem in the distillation of LS is that the boiling temperature of LAB under normal pressure, 275-307 ^{o}C, is much higher than its flash point, 130 ^{o}C [54]. It is possible that LAB may decompose at high temperature. To avoid these problems, we must distill it under very low pressure or vacuum.

In order to study the effectiveness of vacuum distillation, I worked with Dr. X. Dai to assemble an apparatus to spike LS with ^{212}Pb, an apparatus to distill the spiked LS and a counting setup. In our experiment, ^{212}Pb in the Th chain is used to trace the removal efficiency of ^{210}Pb because it is difficult to directly measure ^{210}Pb in LS at very low levels.

3.3.1 Apparatus

Three apparatus systems were used in the experiment to examine the purification by vacuum distillation: ^{212}Pb spike system, LAB vacuum distillation system and β-α delayed coincidence counting system. An ultraviolet and visible spectrometer was also used to examine the absorbance of LAB.

Before the distillation, the LAB was spiked with ^{212}Pb. Figure 3.10 shows the ^{212}Pb spike system. The ^{228}Th spike, about 70 Bq, is adsorbed onto a small hydrous zirconium oxide (HZrO) coated 2 grams of silica gel column and used as the ^{220}Rn source. The gaseous ^{220}Rn was then bubbled into $\sim$35 mL LAB in a test tube for 2-4 hours and decayed to ^{212}Pb, with a half life of 10.6 hours.

Figure 3.11 shows the vacuum distillation apparatus. In addition to what is shown in the picture, a vacuum pump was connected to the system via the pipe indicated. During the distillation, raw LAB was heated in the vaporizing flask under vacuum. The temperature in the flask was monitored by the thermometer and controlled by the heater. Vaporized LAB went through the condenser, which was cooled by water, and was condensed there; then distilled LAB was collected in the collecting flask.

To count the very low level of activity in the raw or distilled LAB, it requires

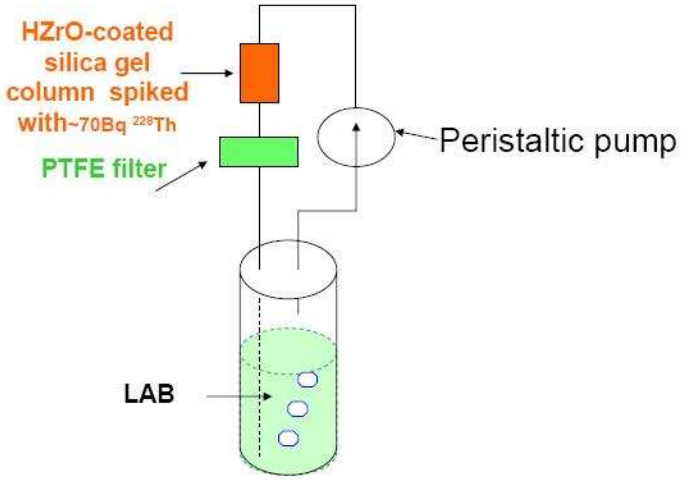

Figure 3.10: Method for spiking with ^{212}Pb radioactivity

Figure 3.11: The set up of the distillation apparatus

counters with high efficiency and low background. The β-α delayed coincidence counting system developed in Oxford for SNO met these requirements[55]. The β decay of ^{212}Bi, the daughter of ^{212}Pb, and the α decay of the ^{212}Po were utilized. The decay scheme is shown in Figure 2.4. There is another series of natural β-α sequential decays, the β decay of ^{214}Bi and the α decay of ^{214}Po in the U chain, as shown in Figure 2.3. The latter sequential decays are easy to exclude because the half-life of ^{214}Po, 164 μs, is much longer than the half-life of ^{212}Po, 300ns.

The samples to be counted were mixed into a liquid scintillator and the β-α decays were counted with a photomultiplier. The $\sim$ 10 mL samples were mixed with 42 g of Optiphase HiSafe 3 liquid scintillator and placed in a 60 mL plastic jar. The jar is made of high radiopurity polymethylpentene. The diameters of the jar and the photomultiplier (an Electron Tubes Ltd 9266XB PMT) are 5 cm. They are optically coupled with silicone grease to maximise light collection. A 2.5 cm thick oxygen-free, high conductivity copper housing is used to shield the counters against soft room gamma rays. There are six counters in the β-α counting system at Queen's University.

Figure 3.12 is the electronics block diagram of a β-α counter. The actual circuit used in our experiment is similar but integrated onto one β-α delayed coincidence electronics unit. All events with coincidences within a 700 μs time window were recorded by the circuit. The following values for each events, TDC, β full-pulse, α full-pulse and α tail-pulse are transferred from the electonics unit to a PC.

A time cut of $\leq$1500 ns on the time T between the β and the α signal was first applied to separate the delayed coincidences in the U chain. In order to reject random coincidences, three offline software cuts were applied. Cross-over coincidences between different counters were removed by a β energy cut, which is normally fixed at 75 keV $\leq\beta\leq$ 2500 keV. Random γ-γ coincidences were greatly reduced by requiring an α energy cut (6 MeV $\leq\alpha\leq$ 14 MeV) and PSD (pulse shape discrimination,

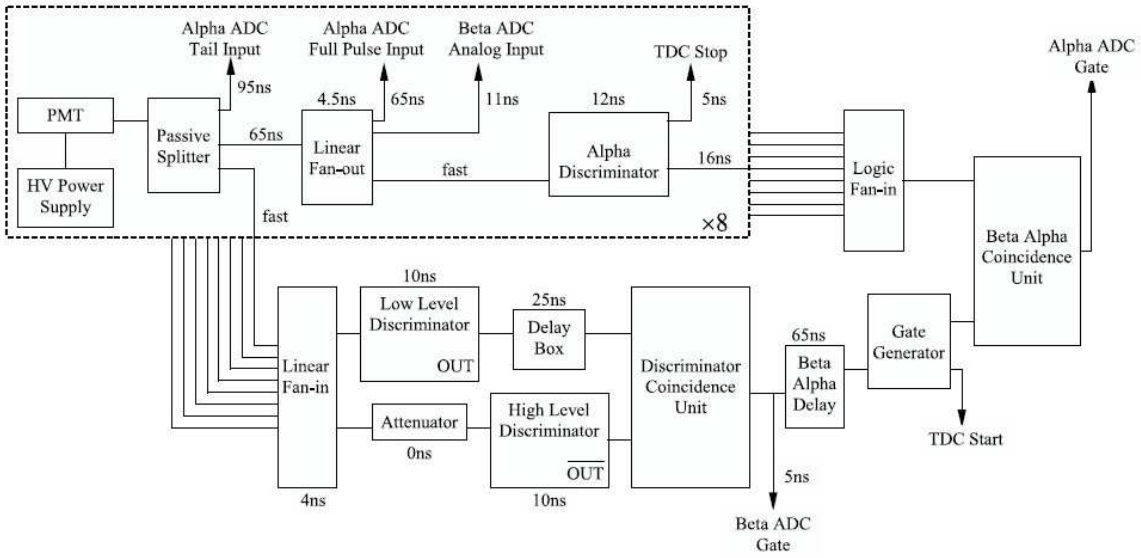

Figure 3.12: Electronics block diagram of the β-α counters [56].

the ratio of the α tail charge/full charge). These three cuts were set using spiked calibration sources. Small shifts in the α peak can occur due to different measurement conditions (including temperature). Therefore, α and PSD cuts were adjusted by the computer software for every individual sample.

The rate of the delayed coincidences was proportional to the activity of ^{212}Bi. This rate varies with time because the radionuclides were not in secular equilibrium. A spectrum of the counting rate plotted against time can be fitted to competing exponentials, and the specific activity of isotopes further up the Th chain including ^{212}Pb can be derived.

The counting efficiency of our β-α counting system for the Th chain activities was calibrated to be 42±2%, using calibration sources with ^{228}Th intensities from 0.0002 to 0.2 Bq.

3.3.2 Procedure

The procedure followed for the purification experiment was:

(1) The LAB was spiked with ^{212}Pb with the spike system shown in Figure 3.10:

After the LAB was spiked, 8-9 grams of the spiked LAB was mixed with 42-43 grams of Optiphase HiSafe 3 cocktail and put into a 60 mL plastic counting pot. This is referred to as liquid scintillator Sample A.

(2) Vacuum distillation:

The rest of the spiked LAB was distilled with the vacuum distillation system shown in Figure 3.11, under a pressure from 40 to 100 microns of Hg and a temperature from 65 ^{o}C to 100 ^{o}C. 8-9 grams were used to make a sample of the purified LAB in the same way as Sample A. This is referred to as Sample B.

(3) Count the ^{212}Pb:

The decays of ^{212}Pb in the two samples were counted simultaneously using two β-α delayed coincidence counters.

3.3.3 ^{212}Pb Reduction Efficiency

In our experiment, the mass of sample A was 8.47g and B was 8.50g. The data of the counters were analyzed. Figure 3.13 shows the counting result of the spiked LAB Sample A and Figure 3.14 shows that of the distilled LAB Sample B. The decay rates of ^{212}Pb of the samples were fitted and shown in the figures. For Sample A, it is 1440 ± 14 counts per hour and for Sample B $1.65^{+0.38}_{-0.34}$ counts per hour. The blank counting rate for this apparatus is about 2^{+2}_{-2} counts per hour. The blank rate is believed to be caused by ^{212}Pb in the air and the large uncertainty is caused by sample variance; in transferring and filling the counting pots there can be variations in the exposure to backgrounds in the air. Because the counting rate of Sample B is low and at the blank level, we take it as an upper limit. Including the uncertainty of the detection efficiency, which is about 5% in total, we calculated a lower limit for the ^{212}Pb reduction efficiency of 99.85%.

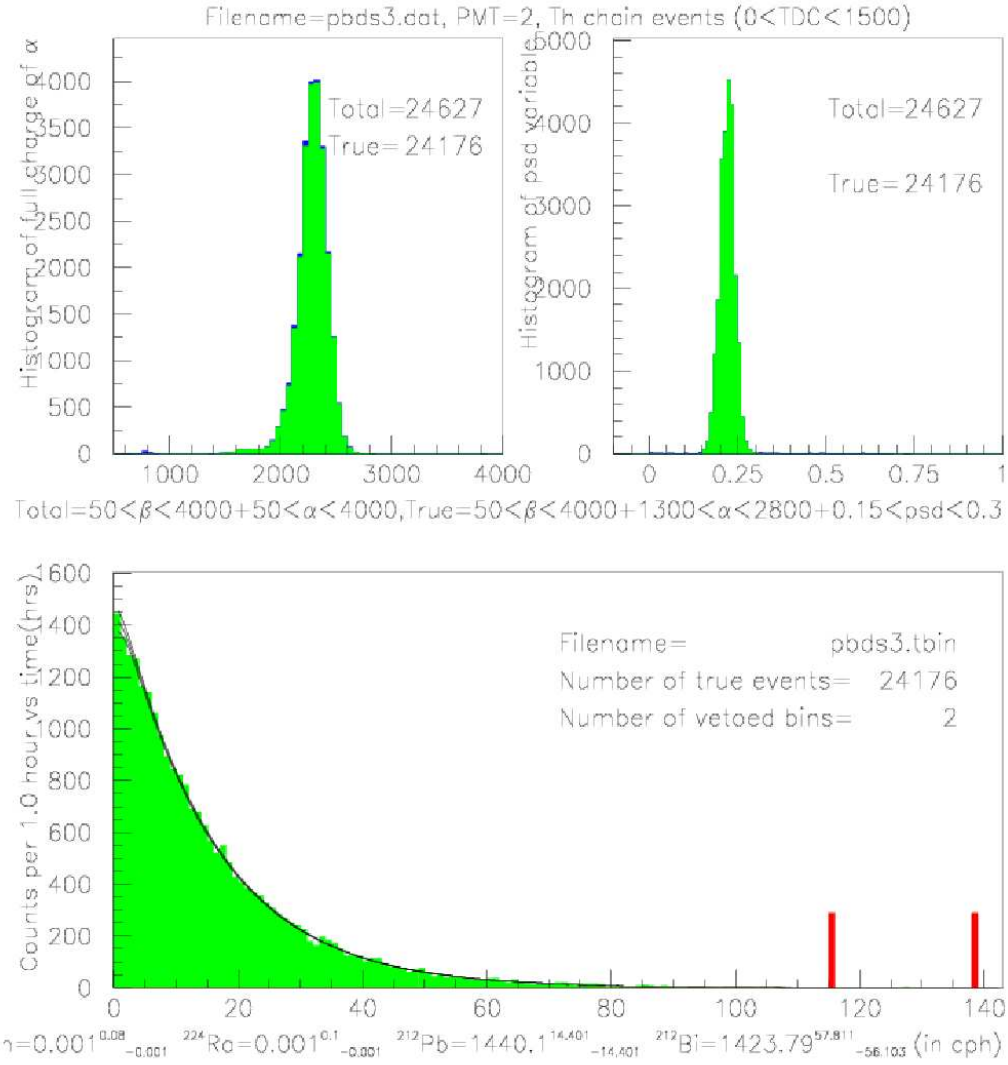

Figure 3.13: The top left is the histogram of the α energy, the top right is the histogram of pulse shape discrimination (ratio of α tail/full charge) and the bottom plot is the counting rate versus time of ^{212}Bi in the spiked LAB sample. The activity of ^{212}Pb was derived by fitting to exponential lifetimes of the parent isotopes that contribute and are shown in the bottom line.

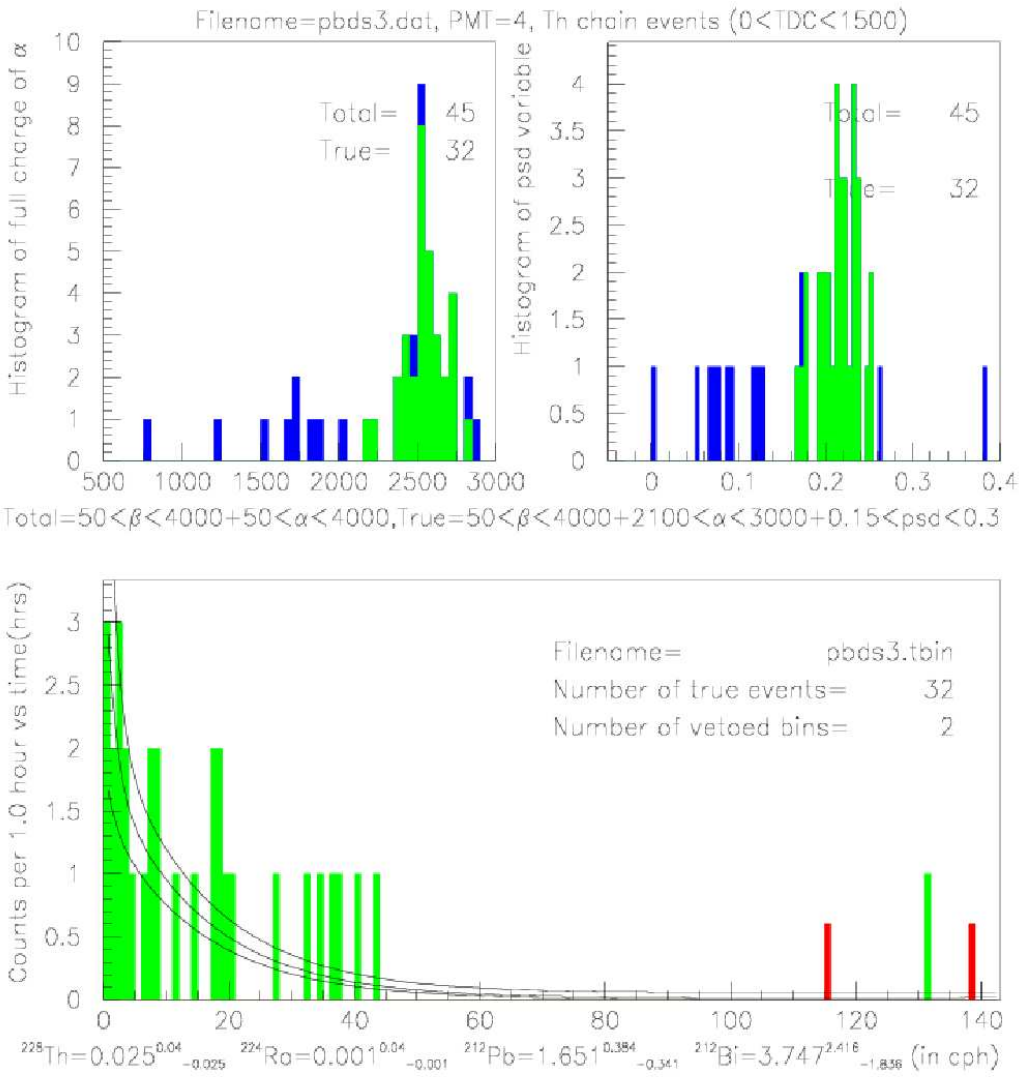

Figure 3.14: The top left is the histogram of the α energy, the top right is the histogram of pulse shape discrimination (ratio of α tail/full charge) and the bottom plot is the counting rate versus time of ^{212}Bi in the distilled LAB sample. The activity of ^{212}Pb was derived by fitting to exponential lifetimes of the parent isotopes that contribute and are shown in the bottom line.

3.3.4 Optical Improvement

The optical absorbance of the LAB was measured with an ultraviolet and visible spectrometer. To cancel the influence of reflection by the walls of the quartz cells, we measured the absorbance of LAB in a 10 cm quartz cell and 1 cm quartz cell. Because the quartz walls of the two cells are the same, the difference between the two measurements is the absorbance of 9 cm LAB without the reflections. The absorbance per centimeter of LAB is

$$\text{Absorbance} = (A_{10cm} - A_{1cm})/(10cm - 1cm) \tag{3.9}$$

The absorbance of the raw LAB and the distilled LAB are shown in Figure 3.15. The absorbance of unit length LAB is reduced by distillation in all wavelengths of concern. The LAB is more transparent after vacuum distillation. The wavelength range having more than 10 m attenuation length extends to about 390 nm from about 450 nm. The bumps between 350 nm and 400 nm become smoother after distillation which indicates that some of the impurities causing these feature peaks are also reduced.

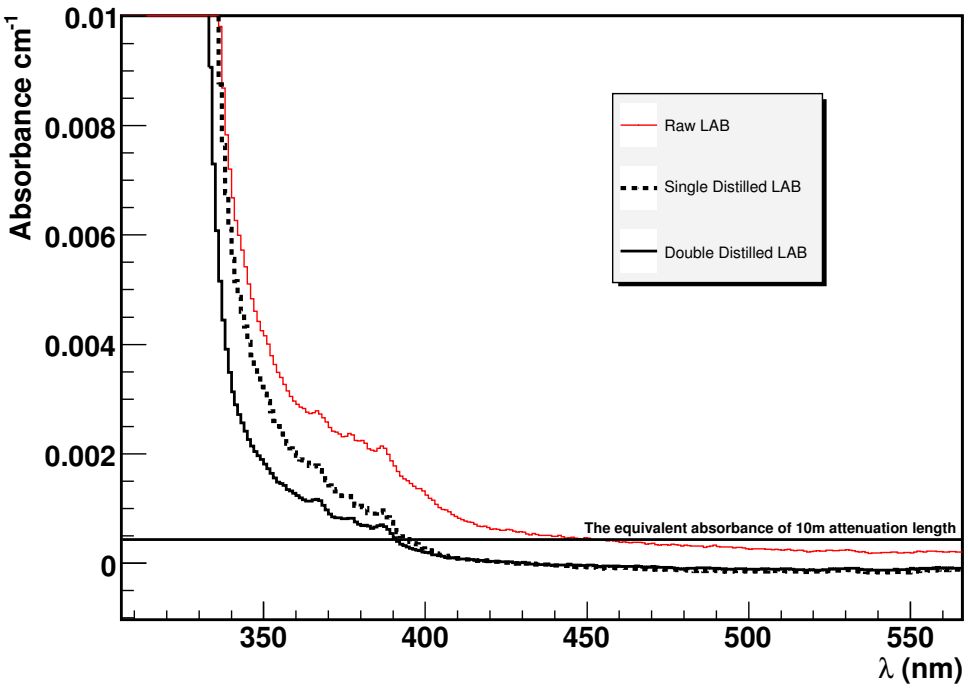

Figure 3.15: The absorbance of raw LAB and distilled LAB

Chapter 4. CONCLUSION

As a successor of SNO, SNO+ will be a good experiment for geoneutrino physics as well as solar neutrino physics, supernova neutrino physics, reactor neutrino physics, and possibly double β decay physics.

Based on the Preliminary Reference Earth Model (PREM) [29] and Crust 2.0 [30], a reference model of the Earth was used for geoneutrino calculations. Using this model, the geoneutrino spectrum and flux at SNOLAB were calculated after studying the distribution of ^{238}U and ^{232}Th, the antineutrino spectra of the two chains and the propagation of antineutrinos in the Earth. The ^{238}U chain geoneutrino flux at SNOLAB is expected to be 3.02×10^6 cm^{-2}s^{-1} and ^{232}Th chain geoneutrino flux is expected to be 2.56×10^6 cm^{-2}s^{-1}. The geoneutrino event rate in SNO+ is expected to be 49 events/10^{32} proton-years.

Background control is vital for SNO+. There are two types of backgrounds, external backgrounds and internal backgrounds. The external background for geoneutrino detection includes the antineutrinos from nuclear plants, neutrons caused by cosmic rays and neutrons from the nuclear reactions in the wall of the cavity. The external neutrons will be shielded by the water around the detector in the cavity and are negligible. Unlike the neutrons, the antineutrinos from nuclear plants can not be shielded. The spectrum and flux of reactor antineutrinos at SNOLAB were calculated. The expected event rate within the energy range from 1.8 MeV to 3.3 MeV is 44 events/10^{32} proton-years. Because the spectrum of reactor antineutrinos is well understood and the higher energy part of the spectrum will be well measured, the

reactor contribution within the energy range from 1.8 MeV to 3.3 MeV can be fitted and separated from the geoneutrino signal.

The internal background for geoneutrino detection is due to (α, n) fake $\bar{\nu}_e$ events. The most significant internal neutron source is $^{13}\mathrm{C}(\alpha, n)^{16}\mathrm{O}$ reaction. If SNO+ achieves the radioactive levels of KamLAND, the (α, n) fake $\bar{\nu}_e$ event rate will be 106 events/10^{32} protons-year, or 78 events/kiloton-year. To reduce this background it is necessary to remove the source of α by purifying the liquid scintillator.^{210}Po, daughter of ^{210}Pb, is the main α source of concern in the SNO+ liquid scintillator. With the method of vacuum distillation, the lead in liquid scintillator can be reduced with an efficiency of at least 99.85%. By using a stronger spiker, it is very likely that the efficiency would be found to be much higher than this number. Purification would reduce fake $\bar{\nu}_e$ event rate to a negligible level. The optical transparency of liquid scintillator is also improved greatly by vacuum distillation, improving SNO+ detector performance.

APPENDIX

Table A.1: Absolute cross section of $^{13}C(\alpha, n)^{16}O$ [47]

E_{eff} (MeV)	σ (mb)	E_{eff} (MeV)	σ (mb)	E_{eff} (MeV)	σ (mb)	E_{eff} (MeV)	σ (mb)	E_{eff} (MeV)	σ (mb)	E_{eff} (MeV)	σ (mb)	E_{eff} (MeV)	σ (mb)
0.767	0.0026	1.588	4.30	2.385	67.5	3.220	67.0	4.065	20.2	4.878	32.9	5.721	227
0.786	0.0033	1.589	6.25	2.395	66.1	3.230	72.1	4.074	20.7	4.888	37.8	5.731	247
0.807	0.0051	1.590	10.5	2.405	65.3	3.239	78.2	4.083	14.8	4.897	44.2	5.740	254
0.826	0.0072	1.591	6.26	2.414	59.8	3.249	85.8	4.092	10.9	4.907	53.0	5.750	256
0.846	0.0108	1.592	4.33	2.424	53.3	3.259	91.9	4.102	8.85	4.917	64.0	5.760	252
0.866	0.0143	1.593	3.32	2.434	45.6	3.269	99.0	4.113	7.96	4.927	80.7	5.770	245
0.886	0.0202	1.595	3.02	2.444	38.6	3.279	104	4.122	7.28	4.937	98.7	5.779	235
0.906	0.0287	1.609	2.12	2.454	34.5	3.289	110	4.132	6.81	4.947	121	5.789	228
0.925	0.0384	1.619	2.17	2.464	32.3	3.299	116	4.142	6.61	4.957	129	5.799	223
0.945	0.0532	1.629	2.23	2.473	28.6	3.309	107	4.152	6.37	4.967	124	5.809	219
0.965	0.0801	1.639	2.29	2.483	26.2	3.319	103	4.162	6.20	4.976	110	5.819	218
0.975	0.0893	1.649	2.38	2.493	24.7	3.329	93.4	4.172	6.19	4.986	95.8	5.829	219
0.985	0.101	1.660	2.45	2.503	23.1	3.338	84.1	4.183	6.10	4.996	90.2	5.839	220
0.994	0.116	1.670	2.75	2.513	21.7	3.348	79.7	4.193	6.03	5.006	92.4	5.850	224

1.005	0.152	1.680	2.85	2.524	21.0	3.358	69.9	4.203	6.07	5.016	93.1	5.860	230
1.016	0.164	1.690	2.95	2.534	20.5	3.368	68.9	4.213	6.17	5.026	95.6	5.870	236
1.025	0.189	1.699	3.24	2.544	20.7	3.378	68.8	4.223	6.23	5.036	99.0	5.880	244
1.030	0.209	1.709	3.34	2.554	21.1	3.388	76.4	4.232	6.43	5.046	103	5.889	265
1.046	0.461	1.719	3.73	2.565	24.7	3.399	88.6	4.242	6.59	5.056	109	5.899	291
1.050	0.850	1.730	4.11	2.576	38.3	3.409	85.6	4.252	6.86	5.066	114	5.909	346
1.052	2.03	1.740	4.30	2.586	51.1	3.418	68.8	4.262	7.15	5.076	119	5.919	389
1.053	4.53	1.749	4.37	2.595	46.2	3.427	48.0	4.272	7.70	5.086	124	5.929	389
1.054	8.77	1.759	4.42	2.602	32.1	3.436	34.7	4.282	8.55	5.096	131	5.939	366
1.055	4.54	1.769	4.81	2.611	24.9	3.446	25.7	4.292	9.70	5.106	137	5.939	401
1.056	2.04	1.779	4.98	2.621	21.5	3.457	20.7	4.302	11.0	5.115	144	5.948	363
1.058	0.880	1.789	5.26	2.632	20.4	3.466	17.1	4.313	13.7	5.125	150	5.958	326
1.062	0.556	1.799	5.48	2.643	22.7	3.476	14.2	4.323	18.1	5.135	165	5.968	272
1.078	0.495	1.808	5.66	2.657	51.8	3.486	12.2	4.333	26.7	5.145	169	5.978	254
1.080	0.481	1.818	5.98	2.666	52.6	3.497	10.6	4.343	43.3	5.155	168	5.988	228
1.087	0.466	1.828	6.42	2.673	39.6	3.507	9.18	4.353	71.7	5.165	167	5.997	209
1.098	0.483	1.839	7.33	2.681	24.1	3.517	7.98	4.362	89.8	5.175	164	6.007	196
1.112	0.485	1.849	7.87	2.690	21.1	3.527	7.09	4.371	76.0	5.185	161	6.018	196

1.122	0.500	1.859	8.33	2.701	19.7	3.537	6.36	4.380	49.6	5.195	157	6.028	208
1.132	0.561	1.869	8.77	2.712	19.6	3.547	5.80	4.389	31.7	5.205	154	6.038	214
1.142	0.598	1.879	9.50	2.723	21.5	3.557	5.21	4.399	22.3	5.215	150	6.048	235
1.152	0.614	1.889	10.1	2.735	35.5	3.567	4.71	4.410	16.9	5.224	146	6.058	296
1.162	0.640	1.899	10.7	2.745	47.5	3.576	4.10	4.420	13.7	5.234	144	6.068	411
1.172	0.664	1.909	11.4	2.754	41.9	3.586	3.60	4.430	12.1	5.244	142	6.079	564
1.182	0.681	1.918	12.3	2.762	31.2	3.596	3.19	4.441	11.4	5.254	141	6.088	628
1.192	0.740	1.928	13.7	2.772	45.9	3.606	2.89	4.451	10.1	5.264	150	6.098	565
1.202	0.749	1.938	14.8	2.787	108	3.618	4.55	4.459	7.70	5.275	201	6.106	466
1.212	0.784	1.948	15.8	2.792	115	3.630	10.2	4.469	6.59	5.284	228	6.116	399
1.222	0.795	1.958	17.3	2.796	108	3.638	9.34	4.480	6.74	5.294	183	6.126	357
1.232	0.796	1.968	18.8	2.801	60.1	3.645	5.85	4.490	7.05	5.303	156	6.136	312
1.242	0.834	1.978	20.5	2.808	30.0	3.655	4.63	4.500	7.51	5.314	151	6.146	280
1.251	0.868	1.988	22.6	2.818	22.6	3.666	4.31	4.510	7.99	5.324	152	6.157	268
1.261	0.869	1.998	24.6	2.830	19.7	3.677	4.97	4.521	10.1	5.333	158	6.167	259
1.271	0.866	2.009	28.0	2.841	18.0	3.691	19.1	4.531	10.9	5.343	168	6.177	263
1.281	0.931	2.019	30.6	2.851	17.1	3.699	33.3	4.541	17.1	5.353	178	6.187	258
1.291	0.887	2.028	33.6	2.862	16.7	3.706	19.4	4.549	55.1	5.363	193	6.197	266

1.301	0.941	2.038	37.0	2.872	16.5	3.713	7.44	4.554	80.7	5.373	211	6.207	267
1.303	0.918	2.048	40.3	2.882	16.5	3.722	4.16	4.558	89.6	5.383	225	6.216	271
1.305	0.930	2.057	43.1	2.892	17.0	3.733	2.75	4.561	76.2	5.393	238	6.226	266
1.307	0.950	2.067	44.2	2.902	17.0	3.744	2.31	4.564	57.7	5.403	243	6.236	265
1.309	0.958	2.077	44.5	2.911	17.3	3.755	2.03	4.568	45.0	5.413	240	6.246	260
1.311	0.990	2.087	48.5	2.921	17.6	3.765	1.72	4.578	37.1	5.423	237	6.256	267
1.333	2.21	2.097	45.2	2.931	18.1	3.775	1.60	4.588	27.4	5.433	235	6.266	274
1.334	4.26	2.106	41.2	2.941	18.7	3.786	1.53	4.598	21.6	5.443	240	6.276	284
1.335	10.8	2.116	39.5	2.951	19.8	3.795	1.50	4.609	20.1	5.452	251	6.286	301
1.336	48.2	2.126	38.2	2.962	21.1	3.805	1.47	4.619	20.2	5.462	254	6.296	314
1.337	10.9	2.136	37.4	2.972	22.1	3.815	1.42	4.629	21.0	5.472	240	6.306	326
1.338	4.27	2.146	37.5	2.982	24.4	3.825	1.39	4.639	22.5	5.482	202	6.316	349
1.339	2.22	2.156	39.8	2.992	27.6	3.835	1.36	4.649	24.2	5.492	173	6.325	356
1.365	1.14	2.167	42.8	3.002	31.9	3.845	1.39	4.659	25.9	5.502	151	6.335	362
1.377	1.13	2.177	47.0	3.012	37.3	3.855	1.37	4.670	28.1	5.512	135	6.345	358
1.389	1.12	2.187	53.0	3.021	41.6	3.865	1.43	4.679	29.3	5.522	123	6.355	344
1.400	1.09	2.197	59.9	3.031	45.8	3.875	1.47	4.688	29.9	5.532	114	6.365	337
1.410	1.11	2.207	66.4	3.041	47.6	3.885	1.57	4.698	30.3	5.542	107	6.375	322

1.420	1.16	2.217	75.2	3.051	46.1	3.895	1.71	4.708	29.8	5.552	101	6.385	308
1.431	1.21	2.227	75.3	3.060	43.8	3.905	1.84	4.718	30.0	5.561	96.6	6.395	296
1.441	1.19	2.236	74.1	3.070	41.2	3.915	2.01	4.728	29.8	5.571	94.1	6.405	273
1.450	1.22	2.245	73.3	3.080	38.8	3.925	2.28	4.738	29.6	5.581	92.0	6.415	261
1.461	1.29	2.255	67.7	3.090	37.4	3.935	2.61	4.748	30.1	5.591	91.1	6.425	255
1.471	1.29	2.265	66.2	3.100	37.3	3.945	2.95	4.758	30.6	5.601	91.3	6.435	246
1.480	1.31	2.275	59.1	3.111	36.9	3.955	3.43	4.768	31.0	5.611	91.8	6.444	243
1.490	1.31	2.285	56.0	3.121	37.0	3.965	4.07	4.778	31.3	5.621	94.0	6.454	244
1.500	1.37	2.295	55.1	3.130	37.9	3.975	4.62	4.787	29.8	5.631	97.3	6.464	246
1.510	1.42	2.305	53.8	3.140	39.2	3.985	5.14	4.797	29.0	5.641	100	6.474	245
1.520	1.44	2.315	53.7	3.150	40.4	3.995	5.62	4.807	27.0	5.651	107	6.484	240
1.530	1.57	2.325	52.9	3.160	42.3	4.005	6.20	4.817	25.5	5.662	115	6.494	241
1.541	1.67	2.335	54.3	3.170	44.4	4.014	6.55	4.827	24.9	5.671	127	6.504	243
1.550	1.62	2.346	56.5	3.180	47.2	4.024	7.05	4.837	24.8	5.681	142	6.514	244
1.560	1.75	2.355	59.0	3.190	52.4	4.034	7.59	4.848	25.8	5.691	163	6.524	245
1.585	2.90	2.365	63.3	3.200	56.9	4.044	8.83	4.858	27.2	5.701	182	6.534	244
1.587	3.20	2.375	66.4	3.210	61.2	4.055	12.5	4.868	29.6	5.711	204	6.544	240

REFERENCES

[1] The SNO Collaboration. Direct evidence for neutrino flavor transformation from neutral-current interactions in the Sudbury Neutrino Observatory. *Phys. Rev. Lett.*, 89, 011301, 2002.

[2] The SNO Collaboration. Electron energy spectra, fluxes, and day-night asymmetries of ^{8}B solar neutrinos from measurements with NaCl dissolved in the heavy-water detector at the Sudbury Neutrino Observatory. *Phys. Rev. C*, 72(5):055502, Nov 2005.

[3] John N. Bahcall, Aldo M. Serenelli, and Sarbani Basu. New solar opacities, abundances, helioseismology and neutrino fluxes. *The Astrophysical Journal*, 621(2):L85–L88, 2005.

[4] S. Enomoto, E. Ohtani, K. Inoue, and A. Suzuki. Neutrino geophysics with KamLAND and future prospects. `hep-ph/0508049`, 2005.

[5] P.Vogel et al. Reactor antineutrino spectra and their application to antineutrino-induced reactions. II. *Phys. Rev. C*, 24, 1543-1553, 1981.

[6] G. Zacek et al. Neutrino-oscillation experiments at the Gösgen nuclear power reactor. *Phys. Rev. D*, 34, 2621-2636, 1986.

[7] The KamLAND Collaboration. First results from KamLAND: Evidence for reactor antineutrino disappearance. *Phys. Rev. Lett.*, 90, 021802, 2003.

[8] The KamLAND Collaboration. Measurement of neutrino oscillation with KamLAND: Evidence of spectral distortion. *Phys. Rev. Lett.*, 94, 081801, 2005.

[9] T. K. Kuo and James Pantaleone. Neutrino oscillations in matter. *Rev. of Modern Phys.*, 61, 937-979, 1989.

[10] M.C. Chen. The SNO liquid scintillator project. *Nucl. Phys. B. (Proc. Suppl.)*, 65:145, 2005.

[11] K. Hirata et al. Observation of a neutrino burst from the supernova SN1987A. *Phys. Rev. Lett.*, 58, 1490-1493, 1987.

[12] R. M. Bionta et al. Observation of a neutrino burst in coincidence with supernova 1987A in the large magellanic. *Phys. Rev. Lett.*, 58, 1494-1496, 1987.

[13] A. Burrows, D. Klein, and R. Gandhi. The future of supernova neutrino detection. *Phys. Rev. D*, 45, 3361-3385, 1991.

[14] C. Lunardini and A. Yu Smirnov. Neutrinos from SN1987A: flavor conversion and interpretation of results. *Astropart. Phys*, 21, 703-720, 2004.

[15] P.J. Kernan and L.M. Krauss. Updated limits on the electron neutrino mass and large angle oscillations from SN1987A. *Nucl. Phys.B*, 437, 243-256, 1995.

[16] C. Hanhart et al. The likelihood of GODs' existence: improving the SN1987A constraint on the size of large compact dimensions. *Phys. Lett. B*, 509:1, 2001.

[17] Alex Wright. PhD thesis proposal, 2005. Internal document.

[18] S.R. Elliott and P. Vogel. Double beta decay. *Annu. Rev. Nucl. Part. Sci.*, 52, 115-151, 2005.

[19] G. Eder. Terrestrial neutrinos. *Nucl. Phys.*, 78, 657-662, 1966.

[20] G. Marx. Geophysics by neutrinos. *Czechoslovak Journal of Physics*, 19, 1471-1479, 1969.

[21] C. Avilez, G. Marx, and B. Fuentes. Earth as a source of antineutrinos. *Phys. Rev. D*, 23,1116-1117, 1981.

[22] L. M. Krauss, S.L. Glashow, and D.N. Schramm. Antineutrino astronomy and geophysics. *Nature*, 310, 191-198, 1984.

[23] M. Kobayashi and Y. Fukao. The Earth as an antineutrino star. *Geophys. Res. Lett.*, 18, 633-636, 1991.

[24] R.S. Raghavan et al. Measuring the global radioactivity in the Earth by multi-detector antineutrino spectroscopy. *Phys. Rev. Lett.*, 80, 635-638, 1998.

[25] C. G. Rothschild, M. C. Chen, and F.P. Calaprice. Antineutrino geophysics with liquid scintillator detectors. *Geophys. Res. Lett.*, 25, 1083-1086, 1998.

[26] F. Mantovani, L. Carmignani, G. Fioretini, and M. Lissia. Antineutrinos from Earth: A reference model and its uncertainties. *Phys. Rev. D*, 69, 013001, 2004.

[27] The KamLAND Collaboration. Experimental investigation of geologically produced antineutrinos with KamLAND. *Nature*, 436, 499-503, 2005.

[28] Gianni Fiorentini, Marcello Lissia, Fabio Mantovani, and Barbara Ricci. Kamland results and the radiogenic terrestrial heat. *Physics Letters B*, 629:77, 2005.

[29] A. M. Dziewonski and D. L. Anderson. Preliminary Reference Earth Model. *Physics of the Earth and Planetary Interiors*, 25, 297-356, 1981.

[30] Gabi Laske, Guy Masters, and Christine Reif. The Reference Earth Model Website. `http://mahi.ucsd.edu/Gabi/rem.html`.

[31] N. Kollerstrom. The hollow world of edmond halley. *Journal for Histrory of Astronomy*, 23, 185-192, 1992.

[32] Sanshiro Enomoto. *Neutrino Geophysics and Observation of Geo-Neutrino at KamLAND*. PhD thesis, Tohoku University, 2005.

[33] T. Plank et al. The chemical composition of subducting sediment: implications for the crust and mantle. *Chemical Geology*, 145, 325-394, 1998.

[34] R. L. Rudnick et al. Nature and composition of the continental crust: A lower crustal perspective. *Rev. of Geophysics*, 33, 267-310, 1995.

[35] S. R. Taylor et al. *The Continental Crust: It's Composition and Evolution*. Blackwell Oxford, 1985.

[36] W. F. McDonough. *Encyclopedia of Geochemistry*. Kluwer Academic Publishers, 1999.

[37] C. Michael Lederer and Virginia S. Shirley et al. *Table of Isotopes, Seventh Edition*. Wiley-Interscience, 1978.

[38] Argonne National Laboratory. International nuclear safety center. `http://www.insc.anl.gov/index.php`.

[39] Nuclear Training Centre at Ljubljana Slovenia. Nuclear power plants all over the world. `http://mtbslovenia.net/plants/`.

[40] Jelena Maricic and Eugene Guillian. Private communication.

[41] P. Vogel. Analysis of the anti-neutrino capture on protons. *Phys. Rev.*, D29:1918, 1984.

[42] Denys H. Wilkinson. Analysis of neutron beta decay. *Nucl. Phys.*, A377:474–504, 1982.

[43] Y. Kishimoto. Liquid scintillator purification, 2004. Presentation at LRT2004.

[44] Nikolai R. Tolich. *Experimental Study of Terrestrial Electron Anti-neutrinos With KamLAND*. PhD thesis, Stanford University, 2005.

[45] R. Heaton, H. Lee, P. Skensved, and B.C.Robertson. Alpha-induced neutron activity in materials. *Nucl. Geophys.*, 4, 499-510, 1990.

[46] R. Heaton, H. Lee, P. Skensved, and B.C.Robertson. Neutron production from thick-target (α, n) reactions. *Nucl. Instr. and Meth. in Phys. Res.*, A276, 529-538, 1989.

[47] S. Harissopulos et al. Cross section of $^{13}\mathrm{C}(\alpha, n)^{16}\mathrm{O}$ reaction: A background for the measurement of geo-neutrinos. *Phys. Rev. C*, 72, 062801, 2005.

[48] J.K. Bair and F.X. Haas. Total neutron yield from the reactions $^{13}\mathrm{C}(\alpha, n)^{16}\mathrm{O}$ and $^{17,18}\mathrm{O}(\alpha, n)^{20,21}\mathrm{Ne}^{+}$. *Phys. Rev. C*, 7, 1356-1364, 1973.

[49] Japanese Evaluated Nuclear Data Library. `http://wwwndc.tokai.jaeri.go.jp/jendl.html`, 2004.

[50] J.K. Bair and H.B. Willard. Level structure in $^{22}\mathrm{Ne}$ and $^{30}\mathrm{Si}$ from the reactions $^{18}\mathrm{O}(\alpha, n)^{21}\mathrm{Ne}$ and $^{26}\mathrm{Mg}(\alpha, n)^{29}\mathrm{Si}$. *Phys. Rev*, 128, 299-304, 1962.

[51] W.H.Bragg and R.Kleeman. *Philos. Mag.*, 10, 318, 1905.

[52] J.F. Ziegler. Particle interactions with matter. `http://www.srim.org`.

[53] G. Both, R. Krotz, K. Lohmer, and W. Neuwirth. Density dependence of stopping cross sections measured in liquid ethane. *Phys. Rev. A*, 28, 3212-3216, 1983.

[54] Petresa Canada Inc. Material safety data sheets, linear alkylbenzene.

[55] R.K. Taplin. *The Use of Photomultipliers in SNO*. PhD thesis, Oxford University, 1995.

[56] T. C. Andersen and the SNO Collaboration. A radium assay technique using hydrous titanium oxide adsorbent for the Sudbury Neutrino Observatory. *Nucl.Instrum. Meth. A*, 501:386, 2003.